ADIABATIC CAPTURE OF NEUTRONS FOR HIGH-BRIGHTNESS BEAMS AND STORAGE OF LOW- AND HIGH-FIELD-SEEKING SPIN STATES

Linh Nguyen

Submitted to the faculty of the University Graduate School

in partial fulfillment of the requirements

for the degree

Master of Science

in the Department of Physics,

Indiana University

December 2023

Accepted by the Graduate Faculty, Indiana University, in partial fulfillment of the requirements for the degree of Master of Science.

Master's Thesis Committee _____

William Michael Snow, Ph.D.

_____

Shyh-Yuan Lee, Ph.D.

_____

Daniel Joseph Salvat, Ph.D.

December 11, 2023

ACKNOWLEDGEMENTS

My first words of gratitude must of course go to my thesis advisor, Professor Emeritus SY Lee. It goes without saying that his experience and expertise have been, and continue to be, invaluable to the field. What perhaps gets far too little attention is that his belief in students has been equally—if not more—valuable. In completing this thesis, I joined the many dozens who have graduated into accelerator physics under his guidance, and it is solely thanks to his unwavering support of students' intellectual journeys that this work was ever able to take shape. A lesser mentor would have expected me to stay in my lane. SY knew what a waste of curiosity and potential that always ends up being with students.

The next set of thanks goes to the US Particle Accelerator School (USPAS), Indiana University Bloomington (IU), and the US Department of Energy Office of High Energy Physics for making this Master's program possible in such a unique and workable format. As someone who had previously earned a Master of Science degree through full-term on-campus courses while working full-time, I never ceased to appreciate the different approach. At USPAS, Susan Winchester, who has been my main point of contact over the years for nearly all matters related to logistics, is especially deserving of thanks. I have no doubt bugged her more than anyone during my time in the program, including SY. Irina Novitski and director Steve Lund also deserve special thanks for their sustained roles in keeping the USPAS gears turning, and while there are too many to name here, I would like to thank all the USPAS instructors and teaching assistants along the way. I learned something from everyone. On the IU side, Professor Mike Snow deserves special thanks for overseeing the program locally and chairing my thesis defense committee. I would like to thank Dr. Daniel Salvat for taking the time to serve on the committee, as well. Nelson Batalon Jr, Anne-Sophie Stringer, and Regan Campbell have assisted me at various points with my IU records, for which I am also grateful.

Last but not least, the Collider-Accelerator Department (C-AD) at Brookhaven National Laboratory deserves tremendous thanks for supporting my completion of the program and accommodating my absence while attending USPAS courses. Owing to the length of my enrollment, the exact roles and times have varied, but it is enough to say that without the consistent approval of Drs. Michiko Minty, Wolfram Fischer, and Thomas Roser, and of Patrick Inacker-Mix, any path through this program would have been very precarious indeed. In addition, within C-AD, Anna Petway and Christina Blas regularly assisted on the administrative side with my travel and reimbursement, and Monica Jackson in the Human Resources Directorate likewise helped make the latter step go like clockwork. Thank you.

Work supported by Brookhaven Science Associates, LLC under Contract No. DE-SC0012704 with the U.S. Department of Energy.

Linh Nguyen

ADIABATIC CAPTURE OF NEUTRONS FOR HIGH-BRIGHTNESS BEAMS
AND STORAGE OF LOW- AND HIGH-FIELD-SEEKING SPIN STATES

The extensive field of accelerator physics furnishes a dizzying array of techniques for the manipulation and storage of charged particles. The neutron, being uncharged, is resistant to nearly all of these techniques but can nevertheless be controlled through its weak magnetic moment to achieve similar qualitative outcomes. The present work adapts the technique of adiabatic capture to neutrons and demonstrates successful neutron beam bunching in simulations. These higher-brightness beams are furthermore achieved in a system that makes no distinction between low- and high-field-seeking spin states when the proper magnet polarities are used, thereby avoiding a prevailing problem in most magnetic neutron storage techniques. The positive results presented suggest that a new set of experimental approaches and tools may be available to improve the outcome of many existing applications of neutron beams, such as scattering studies, and to service the increasingly active field of fundamental neutron physics and low-energy particle physics.

TABLE OF CONTENTS

LIST OF FIGURES

LIST OF TABLES

1 INTRODUCTION

1.1 INTEREST IN THE NEUTRON

The neutron is tremendously important both as an experimental probe and as an experimental subject. The subsections below briefly summarize its historical uses and the active and growing research surrounding it.

1.1.1 Neutron beams and their applications

Intense neutron beams first became available with the construction of nuclear reactors, where channels through the radiological shielding would give access to the high neutron fluxes occurring at the reactor core. The emergence of a new branch of nuclear physics known as neutron optics quickly followed, as did the demand for better neutron sources, and the neutron's immense importance as a tool for studying the internal structure and dynamics of matter has arguably overshadowed its importance as a topic of research in its own right.

Reference [1] provides a comprehensive overview of the ways in which almost all the familiar properties of electromagnetic waves (e.g., reflection, refraction, interference, etc.) can be achieved with neutrons, and outlines the advantages of using neutrons over other means of studying materials, such as electrons and X-rays. The neutron's most obvious advantage over other available particles for scattering experiments is its net electrical neutrality. Its electrical polarizability is also extremely low. As a result, neutrons can

penetrate more deeply into matter at lower kinetic energies and achieve sensitivities many orders of magnitude below the strength of electromagnetic forces. Less obvious perhaps is that the spin states of free neutrons are more easily and efficiently controlled than those of free electrons, giving neutrons the advantage over electrons in demonstrating polarization phenomena. Although X-rays are also uncharged, matter such as light elements, neighboring elements in the periodic table, and different isotopes of the same element cannot be distinguished using X-rays, whereas they are easily distinguishable using neutrons, which primarily probe matter through their nuclear interactions. Neutrons also possess a magnetic moment that can be used to study magnetization in a sample, unlike X-rays.

Spatially, neutron scattering can be used to resolve details as small as 0.1 nm [1], and it constitutes a form of non-destructive testing. Combined with their other measurement capabilities, neutron beams have thus been used in a wide and powerful array of applications demanding high precision, including structural analysis, sample identification, crystal lattice mapping, determination of material properties such as scattering lengths and resonance parameters, investigations into the effect of accelerating fields (in particular, gravity) on matter, determination of domain wall inclinations and separations in ferromagnets, and even the characterization of chirality domains in helimagnets [1]. Neutrons are also used for radiation therapy to treat cancer, but these are typically neutrons with high kinetic energy—at least several MeV [2]. The most sought-after kinetic energy range for neutrons is below 1 eV. ("Neutron energy" will henceforth refer to kinetic energy, unless otherwise noted.) These low-energy neutrons have an especially unique and important feature in that, not only are their de Broglie wavelengths still very well matched to atomic distances (owing to the neutron being heavy), their energies are also very well matched to typical quantized excitation energies of condensed matter (e.g., phonons, magnons, plasmons, etc.) [1]. This combination has made the neutron an unrivalled probe in condensed matter physics

experiments, as it allows neutrons to sample both static and dynamic states of matter—the latter through inelastic scattering.

Neutron beams are also used when studying properties of the neutron itself. These applications will be addressed in the next subsections. In both cases, whether investigating fundamental neutron properties or other matter, neutron beams are limited in their effectiveness by low neutron densities, which can render electrons and X-rays—both producible in very large amounts—more sensitive as probes in many cases, despite their drawbacks. Low neutron densities are detrimental to statistics and incompatible with exposure time limitations, for example. Hence, high intensity is considered the most important requirement for neutron beams [1].

1.1.2 Ongoing investigations into fundamental properties of the neutron

Values for fundamental properties of the neutron appear as inputs or constraints in many important physics equations; their experimental determination therefore serves as critical checks of the underlying laws or theories. One of the most actively researched fundamental properties of the neutron has been its lifetime. The theory of primordial nucleosynthesis (with its understanding of the onset of "nucleon freeze-out" and predictions regarding the subsequent abundances of elements), the weak coupling constants of the Hamiltonian for allowed beta decay in the vector minus axial vector (V-A) standard electroweak model, and the first element of the Cabibbo-Kobayashi-Maskawa (CKM) quark-mixing matrix (and the corresponding checks of unitarity) all rely on the neutron lifetime [3, 4]. More than 20 major experiments have been done on the neutron lifetime since 1950 [3], but the discrepancies that have arisen in the measured value between the different methods employed so far

(beam, material bottle, and magnetic trap) have kept the matter very much open [5], and experiments continue. Magnetic trapping has since become the preferred method, with two recent improved measurements both using magneto-gravitational traps constructed of permanent magnets in a Halbach array [6, 7]. However, a notable aspect of such static magnetic storage techniques (mentioned in both Refs. [6] and [7]) is that, owing to the behavior of neutrons in magnetic fields, only one neutron spin state (up) is trappable for study. This phenomenon will be discussed in more detail in Chapter 2.

Neutron lifetime measurements form a subset of precise measurements involving free neutron beta decay. Other observables appearing in the neutron beta decay rate equation are referred to as correlation coefficients and, of the sixteen correlation coefficients possible, beta asymmetry, electron-antineutrino correlation, the Fierz term, and the two triple correlations have been studied in particular as tests for physics both within and beyond the Standard Model [8]. Previous experiments have investigated limits on scalar and tensor (S and T) coupling and time reversal (T) non-conservation and searched for evidence of right-handed quark currents and spontaneous breaking of Lorentz invariance, among other new physical processes, often relying on neutron beams or high-density "clouds" for their measurements [8].

Lastly, the possible existence of a permanent neutron electric dipole moment (EDM) has also remained a highly active area of research since around 1950 [9]. A nonzero value would provide direct evidence of T symmetry violation, as well as of combined charge conjugation and parity (CP) violation, while the level of sensitivity would test or constrain many models, including the Standard Model and models of baryon asymmetry [9]. As above, neutron EDM searches involve free neutrons, albeit at the lowest possible energies (< 200 neV), unlike scattering studies. At these energies, neutron densities are even lower, and reported effective equilibrium densities of 2 to 5 neutrons per cm^3 are typical for experiments

[9, 10]. Given the shot noise dependence on the total number of neutrons counted, an increase in neutron density is required to increase the sensitivity of experimental searches [9].

1.1.3 The growing field of low-energy particle physics

Although many of the scientific areas described above can be categorized as topics in neutron particle physics, they are strikingly not in the realm of high-energy physics, which is so often associated with particle physics due to the high visibility of particle colliders. The neutron plays a central role in the emerging low-energy frontier of particle physics. Reacting to all known forces, it enables a vast array of investigations. Reference [11] provides a comprehensive early look at the opening landscape of low-energy particle physics with the neutron, while Refs. [12] and [4] provide updates on progress, outstanding problems, and measurement sensitivities—the former reporting 10^{-23} eV for energy resolution and 10^{-11} for relative uncertainties in atomic masses and neutron momentum transfer. As described in these references, in addition to the topics already covered, low-energy particle physics with the neutron can address questions related to baryon number non-conversation (via neutron-antineutron oscillations), lepton number non-conservation (via reactor-neutrino oscillations), parity non-conservation (via neutron-nuclear interactions), the existence of axions, improvements in the value of the fine structure constant, dressed particle effects, geometric (Berry) phases in quantum systems, the foundations of quantum mechanics (via neutron interferometry), supersymmetric models (via EDM constraints), the equivalence principle in the quantum limit, gravity-induced quantum interference, bound quantum states in the gravitational potential, non-Newtonian gravity, dark matter, rare Standard Model decay channels, and quantum chromodynamics (QCD). The search for neutron-antineutron

oscillations, which involves observing a large number of low-energy neutrons over a long time of flight, in particular has been noted as awaiting increases in total neutron beam intensity to improve upon previously established upper bounds on the oscillation time [12, 13]. In general, the development of new types of low-energy neutron sources and increases in neutron fluences has paved the way for new experiments and scientific areas [4]. Reference [8] discusses the comparable limits of low- and high-energy experiments and how the two regimes complement one another in the search for new physics beyond the Standard Model.

1.2 MOTIVATIONS FOR THE PRESENT WORK

In the summary above, two experimental aspects are specifically remarked upon: the benefits of achieving ever greater low-energy neutron densities and the unequal footing of up and down spin states in certain storage techniques. The present work, which concerns the adiabatic capture of neutron beams for neutron beam bunching, most clearly addresses the former by exploring the extension of a method already demonstrated with charged particles—such as in the Cooler Injector Synchrotron (CIS) ring at the Indiana University Cyclotron Facility (IUCF) [14]—to neutral particles with a magnetic moment. The outcome is a bunched neutron beam of greater brightness than the initial beam. The term “brightness” is used for the present work owing to its correspondence to density in phase-space, which is the treatment pursued. Transverse phase space is generally implied by this term—beam brightness being equal to beam current divided by transverse beam emittance—but while the adiabatic capture process studied in this work occurs in longitudinal phase space, it should be clear that it also occurs within the larger context of storage ring accelerator physics

and lattice design, where transverse emittance is a basic figure of merit that attends the entire machine. Hence, greater neutron density is a less stringent outcome. In applications where angular spread is not of much importance, “high-brightness” can simply be taken to mean “high-density”.

As will be seen in Chapter 4, the present work focuses on the adiabatic capture of neutrons with energies around 1 μeV—with higher energies being possible, albeit at the cost of more demanding magnets and larger rings. Such neutrons can be produced in much greater quantity than those required for the material bottle and magnetic trapping techniques described above; thus, the present work is also partly motivated by the possibility of greatly extending the working energy range of stored neutrons, which would improve neutron beam densities as a matter of course.

On the topic of existing magnetic storage techniques, the present work moreover seeks to avoid the problem of rejecting spin-down neutrons; accepting both spin states is achievable in the system put forth by the switching of magnet polarity. This ensures a symmetric benefit in brightness gains and makes available either spin state for experiments related to spin-dependent physics.

Lastly, the rather sweeping review of neutron physics experiments in the preceding section does not mean to suggest that the present work will be beneficial or even applicable to all the topics discussed. Instead, it highlights the breadth and expanding opportunities in the field, while also touching on its comparatively small community. This fact alone makes any additional attention worthwhile and the impact and uses of any new tools hard to predict. On a final note, then, the present work hopes to aid in the growing interest in the neutron and low-energy physics.

2 THE PHYSICS OF SLOW NEUTRONS

2.1 NEUTRON ENERGY SPECTRUM

Although neutrons must first be liberated from nuclei via high-energy reactions before they can be used in experiments, mechanisms for lowering their energy following liberation are many (see, for example, Refs. [1] and [12] for an overview). As a result, the range of neutron energies available for experimenters is vast, ranging from several MeV down to peV [12]. "Temperature" is used to describe and make finer distinctions among the class of "slow"—that is, sub-eV—neutrons. These neutrons are typically divided into epithermal, thermal, cold, very cold, and ultracold; however, there is some variation in the subgroups and their energy ranges among sources. For example, Ref. [4] uses 500 keV as the upper boundary for epithermal neutrons. Meanwhile, other sources omit the "very cold" subgroup (e.g., Ref. [8]).

The present work will ascribe to the classification system presented in Ref. [1]. Accordingly, slow neutrons are grouped as in Table 2.1. It is clear from the velocities listed that a non-relativistic treatment of the physics concerned will suffice throughout. As explained in the same reference, the transition from epithermal to thermal neutrons is characterized by a change in the nature of the collection's energy distribution, with epithermal flux having a distribution that varies inversely with energy and thermal flux exhibiting the Maxwellian distribution belonging to a system in thermal equilibrium with its surroundings. The 25 meV of energy of a thermal neutron, therefore, corresponds to a neutron in thermal equilibrium at 300 K. The topic of the Maxwellian distribution of thermal neutrons will be revisited later in Section 4.3.3, as part of the discussion on simulation results.

Term	Energy	Approx. velocity (m/s)
epithermal	25 meV < E ≤ 1 eV	2200 < v ≤ 13800
thermal	$E \simeq 25$ meV	$v \simeq 2200$
cold	50 μeV ≤ E < 25 meV	100 ≤ v < 2200
very cold	200 neV ≤ E < 50 μeV	6 ≤ v < 100
ultracold	E < 200 neV	v < 6

Table 2.1: Slow neutron energy spectrum

2.2 THE NEUTRON MAGNETIC MOMENT

The neutron's lack of an electric charge—confirmed experimentally down to the order of 10^{-22} electron charges [12]—has meant that experimentalists have often relied on its magnetic properties for manipulation. The neutron possesses an intrinsic magnetic moment μ_n roughly two-thirds that of the proton and, in terms of the nuclear magneton μ_N, the value is given by

$$\mu_n = -1.91304\,\mu_N \tag{2.1}$$

where

$$\mu_N = \frac{e\hbar}{2m_p} \tag{2.2}$$

in SI units. In the equation, $e = 1.60218 \times 10^{-19}\ C$ is the elementary charge, $\hbar = {}^{h}/_{2\pi} = 1.05457 \times 10^{-34}\ J \cdot s$ is the reduced Planck's constant, and $m_p = 1.67262 \times 10^{-27}\ kg$ is the mass of the proton. The currently accepted numerical value of the neutron magnetic moment [15] is

$$\mu_n = -9.66237 \times 10^{-27}\ J/T = -6.03076 \times 10^{-10}\ eV/T$$

For comparison, the neutron's mass m_n being $1.67493 \times 10^{-27}\ kg$, its gravitational interaction $m_n g$, where $g = 9.8\ m/s^2$, is on the order of $10 \times 10^{-10}\ eV/m$. The similar scales mean that the effects of Earth's gravity are non-negligible in the regime to be considered; however, this matter will only be taken up at the end of this thesis, in Chapter 5, as it does not affect the axis that is the main focus of the present work (i.e., the longitudinal axis).

2.3 NEUTRON SPIN AND SPIN BEHAVIOR IN FIELDS

The neutron is a fermion with a spin of $\frac{1}{2}$; Ref. [13] nicely summarizes the support for this value. This means that the neutron spin operator, as with all spin-$\frac{1}{2}$ particles, can be written as

$$\boldsymbol{S} = \frac{\hbar}{2}\boldsymbol{\sigma} \tag{2.3}$$

where $\boldsymbol{\sigma}$ are the Pauli spin matrices

$$\boldsymbol{\sigma}_1 = \begin{pmatrix} 0 & 1 \\ 1 & 0 \end{pmatrix}, \quad \boldsymbol{\sigma}_2 = \begin{pmatrix} 0 & -i \\ i & 0 \end{pmatrix}, \quad \boldsymbol{\sigma}_3 = \begin{pmatrix} 1 & 0 \\ 0 & -1 \end{pmatrix} \tag{2.4}$$

all with eigenvalues $+1$ and -1. This gives $\boldsymbol{S}$ the eigenvalues $+\frac{\hbar}{2}$ and $-\frac{\hbar}{2}$.

An alternative formula for the neutron magnetic moment can therefore be written using $\boldsymbol{S}$. In this case,

$$\boldsymbol{\mu}_n = -1.91304\,\boldsymbol{\mu}_N = -1.91304\left(\frac{e}{m_p}\right)\boldsymbol{S} \tag{2.5}$$

If we impose a magnetic field $\boldsymbol{B}$ entirely along one direction, then the spin of a neutron under adiabatic conditions in that field will also lie entirely along that direction [1]. The potential energy that the neutron possesses in that configuration is given by

$$U = -\boldsymbol{\mu}_n \cdot \boldsymbol{B} = \begin{cases} \mu_n|\boldsymbol{B}|\cos\theta\,, & \text{for } S = +\dfrac{\hbar}{2} \\ -\mu_n|\boldsymbol{B}|\cos\theta\,, & \text{for } S = -\dfrac{\hbar}{2} \end{cases} \tag{2.6}$$

where θ is the smallest angle between $\boldsymbol{\mu}_n$ and $\boldsymbol{B}$. We immediately see that the potential energy takes its most negative value when $\theta = \pi$ for $S = +\frac{\hbar}{2}$ and $\theta = 0$ for $S = -\frac{\hbar}{2}$.

Since spin-up states correspond to $+\frac{\hbar}{2}$ and spin-down states to $-\frac{\hbar}{2}$, this result accounts for the manner in which a neutron's spin orients itself in an external magnetic field: the spin of a neutron will tend to align with or anti-align with the field depending on whether it is in the down state or up state, respectively. Moreover, in the presence of field gradients, minimization of potential energy will cause spin-up neutrons to seek local minima, while spin-down neutrons will seek local maxima. If their kinetic energy is much less than $|\mu_n B|$, anti-aligned (spin-up) neutrons will reflect upon encountering a region of higher field, while aligned (spin-down) neutrons will be accelerated into the region [16]. Hence, in the literature, spin-up neutrons are referred to as "low-field seekers" and spin-down neutrons are referred to as "high-field seekers".

Although quasistatic magnetic fields cannot exhibit local maxima in vacuum away from sources or currents to trap high-field seekers, time-varying magnetic fields can. Reference [16] presents the first observation of this phenomenon. In the described experiment, a magnetic field is ramped in the air gap of a split coil magnet that surrounds a vertically oriented guide for ultracold neutrons. As the field ramps up, a local field maximum is formed in the air gap, and low-field seekers are accelerated out. High-field seekers, meanwhile, are decelerated and remain inside.

As will be explored later, a time-varying (ramping) magnetic field will likewise be exploited in the present work to enable the storage of either high- and low-field seeking neutrons. For now, a point must be made regarding the adiabatic condition that Ref. [16] takes care to address. This condition is given by

$$\frac{\left|\frac{dB_\perp}{dt}\right|}{B} = \frac{\left|\frac{dB_\perp}{dx}\right|\left|\frac{dx}{dt}\right|}{B} \ll \omega_L \tag{2.7}$$

where dx/dt is the neutron's velocity and ω_L is the Larmor frequency of the neutron spin:

$$\omega_L = \frac{2\mu_n}{\hbar} B \tag{2.8}$$

In regions where the magnetic field is zero or near zero, this condition can become restrictive enough that nonadiabatic (Majorana) spin-flip transitions are likely, such as in certain magnetic trap configurations [17, 18]. In setting forth the present work, the use of sudden field transitions into and out of zero-field regions (used to achieve the magnetic shielding required for a neutron to experience net energy gain in the time-varying field, as discussed in the next chapter) may at first glance seem to violate the above adiabatic condition and thus repeatedly induce severe depolarization. However, a step-function-like behavior in the field at these locations is sought in the longitudinal direction only; the transverse field, on the

contrary, must be designed to be as gradient-free as possible throughout the system. The restriction on field gradients in Eq. (2.7) is in the transverse direction. It should also be noted that an identical problem ought to plague charged particle accelerators and storage rings if such transverse fringe fields could appreciably cause depolarization. That polarized programs in circular colliders are indisputably viable [19] despite the sheer number of particle passages through field-free regions per turn per second supports the case that the insertion of these regions in the proposed manner will not cause significant depolarization.

3 NEUTRON BEAM STORAGE

3.1 NEUTRONS IN AN APPLIED MAGNETIC FIELD

In this thesis, the term "magnetic field" has hitherto been used to refer to the field symbolized by $\boldsymbol{B}$ —this is, in fact, the vector field traditionally known as the magnetic flux density (or magnetic induction), while $\boldsymbol{H}$, which is equal to $\boldsymbol{B}/\mu_0$ in vacuum, is the magnetic field strength (or magnetic field intensity). This initial word choice was made in keeping with the language used in the cited sources; however, this thesis will henceforth refer to $\boldsymbol{B}$ as the "B-field" to avoid the associated ambiguity without becoming needlessly verbose.

The present work deals with neutrons traveling in vacuum. Maxwell's Equations in vacuum, in SI units, are

$$\boldsymbol{\nabla} \cdot \boldsymbol{E} = \frac{\rho}{\varepsilon_0} \tag{3.1a}$$

$$\boldsymbol{\nabla} \cdot \boldsymbol{B} = 0 \tag{3.1b}$$

$$\boldsymbol{\nabla} \times \boldsymbol{E} = -\frac{\partial \boldsymbol{B}}{\partial t} \tag{3.1c}$$

$$\boldsymbol{\nabla} \times \boldsymbol{B} = \mu_0 \boldsymbol{J} + \mu_0 \varepsilon_0 \frac{\partial \boldsymbol{E}}{\partial t} \tag{3.1d}$$

where the permittivity of free space ε_0 is equal to $8.854 \times 10^{-12}\ F/m$ and the permeability of free space μ_0 is $4\pi \times 10^{-7}\ T \cdot m/A$. For charged particle beams, Eqs. (3.1a) and (3.1d) retain source terms ρ and $\boldsymbol{J}$; however, owing to the electrical neutrality of the neutron, the source terms vanish, and the equations simplify to

$$\boldsymbol{\nabla} \cdot \boldsymbol{E} = 0 \tag{3.2a}$$

$$\boldsymbol{\nabla} \cdot \boldsymbol{B} = 0 \tag{3.2b}$$

$$\boldsymbol{\nabla} \times \boldsymbol{E} = -\frac{\partial \boldsymbol{B}}{\partial t} \tag{3.2c}$$

$$\boldsymbol{\nabla} \times \boldsymbol{B} = \mu_0 \varepsilon_0 \frac{\partial \boldsymbol{E}}{\partial t} \tag{3.2d}$$

The neutron's magnetic moment will interact with the transverse components of an applied B-field in the following manner: a torque will be exerted in proportion to the magnetic moment and the field, or

$$\boldsymbol{\tau} = \boldsymbol{\mu}_n \times \boldsymbol{B} \;\; \rightarrow \;\; |\boldsymbol{\tau}| = |\boldsymbol{\mu}_n||\boldsymbol{B}| \sin\theta \tag{3.3}$$

where θ is the smallest angle between $\boldsymbol{\mu}_n$ and $\boldsymbol{B}$. The potential energy associated with this torque is

$$U = \int_0^{\theta} |\boldsymbol{\tau}| \, d\theta' = |\boldsymbol{\mu}_n||\boldsymbol{B}| \int_0^{\theta} \sin\theta' \, d\theta' = -|\boldsymbol{\mu}_n||\boldsymbol{B}| \cos\theta + |\boldsymbol{\mu}_n||\boldsymbol{B}| = -\boldsymbol{\mu}_n \cdot \boldsymbol{B} \tag{3.4}$$

We have ignored the $|\boldsymbol{\mu}_n||\boldsymbol{B}|$ term since it constitutes a constant in the potential energy, and $-|\boldsymbol{\mu}_n||\boldsymbol{B}| \cos\theta = -\boldsymbol{\mu}_n \cdot \boldsymbol{B}$. This is the origin of Eq. (2.6).

The total change in energy ΔE experienced by the neutron as it travels through the field is found by integrating over the work done by the field:

$$\Delta E = W = \int_a^b \boldsymbol{F} \cdot d\boldsymbol{r} \tag{3.5}$$

Furthermore,

$$\boldsymbol{F} = -\boldsymbol{\nabla} U \tag{3.6}$$

If we restrict the neutron's motion to one direction, called the s-direction (defined in the next section), and choose the polarity correctly for the spin state, then the integral takes the form

$$\Delta E = \int_a^b -\frac{\partial U}{\partial s} ds = \int_a^b -\frac{\partial(-\boldsymbol{\mu}_n \cdot \boldsymbol{B})}{\partial s} ds = \mu_n \int_a^b \frac{\partial(\boldsymbol{B})}{\partial s} ds \tag{3.7}$$

Note that, if $\boldsymbol{B}$ is a well-defined function, then so are $\frac{\partial(\boldsymbol{B})}{\partial s}$ and $B_s(s) = \int \frac{\partial(\boldsymbol{B})}{\partial s} ds$. ΔE then takes the value $\mu_n[B_s(b) - B_s(a)]$ regardless of the behavior of $\partial(\boldsymbol{B})/\partial s$ between a and b. Evaluating the integral over any interval where $B_s(a) = B_s(b)$ will result in zero net energy change. Figure 3.1(a) shows this case: the energy gained by a neutron going from s_1 to s_2, when not attended by a spin flip at s_2, is canceled by the energy lost going from s_2 to s_3 because $B_s(s_1) = B_s(s_3)$ means $B_s(s_2) - B_s(s_1) = -[B_s(s_3) - B_s(s_2)]$. The case for $B_s(s_1) = B_s(s_3) = 0$ happens to be shown, but it would also apply if $B_s(s_1)$ and $B_s(s_3)$ were equal to an arbitrary constant.

However, now let us consider the field shown in Fig. 3.1(b). It shows the field suddenly vanishing at s′, just past s_2. Mathematically, a near-instantaneous transition such as this can be modeled by $B_s(s_2)[1 - \Theta(s - s')]$, where $\Theta(s)$ is the Heaviside step function and $B_s(s_2)$ determines the height of the step. The derivative of $\Theta(s)$ is the Dirac delta function $\delta(s)$; the derivative of $B_s(s_2)[1 - \Theta(s - s')]$ is therefore $-B_s(s_2)\delta(s - s')$. Substituting this into Eq. (3.7), we get, in the vicinity of the step,

$$\Delta E = \mu_n \int_a^b \frac{\partial(\boldsymbol{B})}{\partial s} ds = -\mu_n B_s(s_2) \int_a^b \delta(s - s')\, ds \tag{3.8}$$

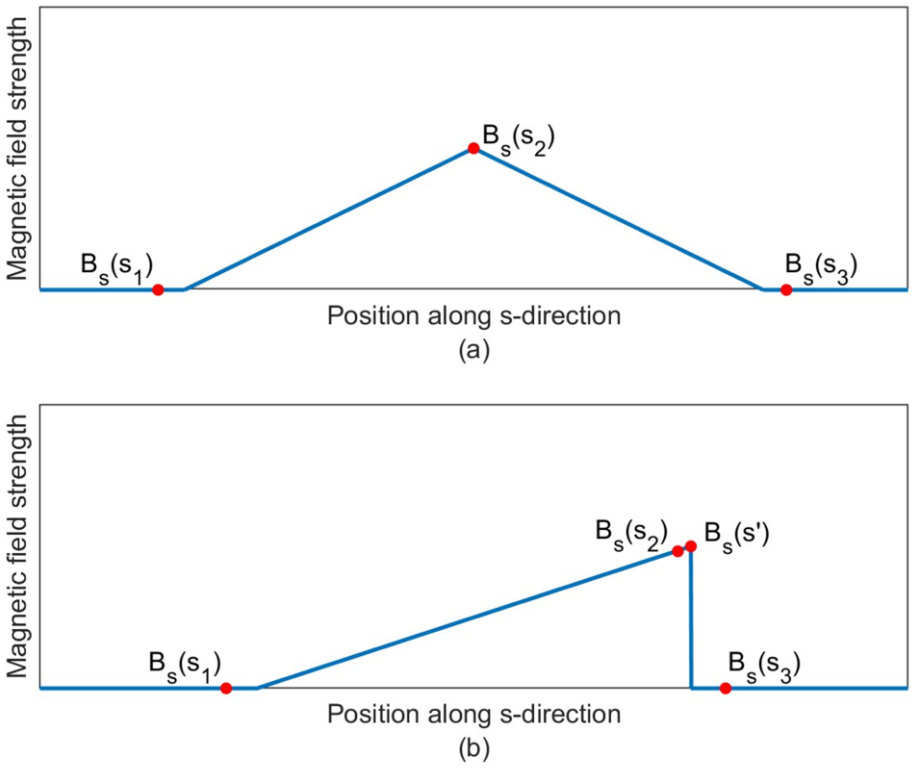

Figure 3.1: Two different magnetic field ramps: (a) a ramp described by a well-defined function and (b) a ramp terminating in an idealized step. For the ramp to be single valued at s', it is treated mathematically like the Heaviside step function $\Theta(s-s')$, with derivative $\delta(s-s')$, in the vicinity of s', but then it is discontinuous.

Strictly speaking, this would evaluate to $-\mu_n B_s(s_2)$ since $\int_a^b \delta(s-s')ds = 1$ as long as s' is in the interval between a and b. When added to the gain in energy $+\mu_n B_s(s_2)$ (since $B_s(s_1) = 0$) in the interval between s_1 and s_2, this would appear to lead to the same null result as above. However, $\delta(s-s') = 0$ everywhere except at *exactly* s', and physically the neutron is traveling with some velocity v wherein the time Δt spent in the gradient of the step goes to zero. Hence, we conclude that the integral substantially evaluates to zero for a physical system.

That a neutron's energy will remain substantially unaffected by field transitions that can be treated as step functions will be invoked later when discussing the magnetic insulation present in the proposed apparatus.

3.2 NEUTRON STORAGE RING DYNAMICS

3.2.1 Frenet-Serret coordinate system

The present work will use the established coordinate system, known as the Frenet-Serret coordinate system, of accelerator physics [20]. It is a curvilinear coordinate system that moves with an idealized "design particle" along a reference orbit $\boldsymbol{r}_0(s)$, where s is the path length along the reference orbit relative to some initial point $\boldsymbol{r}_0(0)$. The instantaneous direction of s is then given by the unit vector tangent to $\boldsymbol{r}_0(s)$, found by taking the derivative of $\boldsymbol{r}_0(s)$ with respect to s:

$$\hat{\boldsymbol{s}}(s) = \frac{d\boldsymbol{r}_0(s)}{ds} \tag{3.9}$$

The unit vector perpendicular to $\hat{\boldsymbol{s}}(s)$ but remaining in the plane of the reference orbit is designated $\hat{\boldsymbol{x}}(s)$:

$$\hat{\boldsymbol{x}}(s) = -\rho(s)\frac{d\hat{\boldsymbol{s}}(s)}{ds} = -\frac{1}{\kappa(s)}\frac{d\hat{\boldsymbol{s}}(s)}{ds} \tag{3.10}$$

$\hat{\boldsymbol{s}}(s)$ and $\hat{\boldsymbol{x}}(s)$ span the so-called osculating plane [21]. $\rho(s)$ is the local radius of curvature of the osculating circle that approximates the curve segment and $\kappa(s)$, which is the reciprocal

of $\rho(s)$, is called the curvature. The convention in differential geometry is for $\hat{\boldsymbol{x}}(s)$ to point towards the center of the osculating circle; the convention in accelerator physics, however, is for $\hat{\boldsymbol{x}}(s)$ to point away from it, such that values of $x > 0$ are at a greater distance from the center than the design particle. This is the source of the negative sign.

The remaining unit vector, which is orthogonal to the osculating plane, is typically denoted as $\hat{\boldsymbol{y}}(s)$ or $\hat{\boldsymbol{z}}(s)$; this thesis will use $\hat{\boldsymbol{y}}(s)$. For a right-handed orthonormal coordinate system in $(\hat{\boldsymbol{x}}, \hat{\boldsymbol{s}}, \hat{\boldsymbol{y}})$, it is straightforward to write down its definition:

$$\hat{\boldsymbol{y}}(s) = \hat{\boldsymbol{x}}(s) \times \hat{\boldsymbol{s}}(s) \tag{3.11}$$

See Fig. 3.2.

For simplicity, we will ignore torsion, which is a measure of how much a curve is tending to deviate from the osculating plane. This is equivalent to restricting our reference orbit to a plane curve, rather than generalizing it to space curves [16]. With this simplification, the motion of an arbitrary particle in the system is given by the position vector

$$\boldsymbol{r}(s) = \boldsymbol{r}_0(s) + x\hat{\boldsymbol{x}}(s) + y\hat{\boldsymbol{y}}(s) \tag{3.12}$$

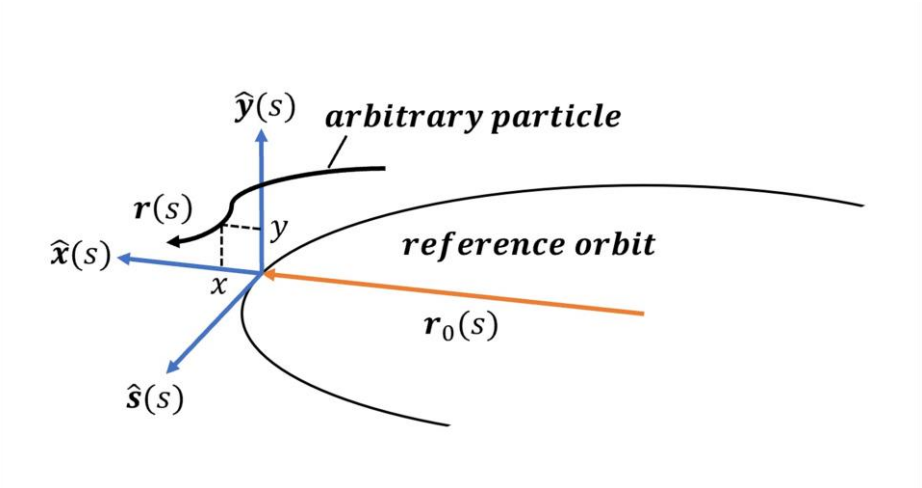

Figure 3.2: Frenet-Serret coordinate system

Note that $\boldsymbol{r}(s)$ is implicitly parameterized by time t as the independent variable since, in the systems under consideration, $s = s(t)$.

3.2.2 Hamiltonian mechanics

The Hamiltonian formulation allows us to immediately write down equations of motion for a system of particles in terms of generalized coordinates q_i if we know the Lagrangian of the system. Noting that this thesis will switch the definition of U and V as given in Ref. [22] (wherein a derivation of what follows can be found) in order to remain internally consistent with variables, the Lagrangian L is equal to the difference between the system kinetic energy T and potential energy U:

$$L = T - U \tag{3.13}$$

The Lagrangian will depend on the generalized coordinates q_i, velocities $\dot{q}_i$, and t: $L = L(q_i, \dot{q}_i, t)$. For a system with n degrees of freedom, $i = 1, 2, \dots, n$. As with elsewhere in this thesis, the dot above a variable denotes a derivative with respect to time. Furthermore, L will satisfy the equation

$$\frac{d}{dt}\left(\frac{\partial L}{\partial \dot{q}_i}\right) - \frac{\partial L}{\partial q_i} = 0 \tag{3.14}$$

From here, conjugate momenta p_i can be found (there is no sum over k):

$$p_i(q_k, \dot{q}_k, t) = \frac{\partial L(q_k, \dot{q}_k, t)}{\partial \dot{q}_i} \tag{3.15}$$

Performing a Legendre transformation on the Lagrangian, which accomplishes the change in variables from $(q, \dot{q}, t)$ to (q, p, t) when p, q, and $\dot{q}$ are related through Eq. (3.15) [22], we arrive at the Hamiltonian

$$H = \sum_{i=1}^{n} P_i \dot{q}_i - L(q_k, \dot{q}_k, t) \tag{3.16}$$

and the equations of motion

$$\dot{q}_i = \frac{\partial H}{\partial p_i} \quad , \quad \dot{p}_i = -\frac{\partial H}{\partial q_i} \tag{3.17}$$

The variables q_i and p_i are known variously as canonical variables and canonically conjugate pairs.

In Section 3.2.5, we will derive longitudinal equations of motion and a Hamiltonian for the proposed system from an analysis of a "synchronous" particle traveling through it, rather than from knowledge of the system Lagrangian. However, we need to express the equations of motion above in terms of our Frenet-Serret coordinate system, which requires knowing the conjugate momenta in Cartesian coordinates and hence the Lagrangian in Cartesian coordinates. Conventionally, lower-case conjugate variables $(\boldsymbol{q}, \boldsymbol{p})$ are used to denote old variables and upper-case conjugate variables $(\boldsymbol{Q}, \boldsymbol{P})$ are the new variables following a transformation. In order to end up with the lower-case variety as our canonical variables for use throughout the remainder of this thesis, we start by letting $(\boldsymbol{Q}, \boldsymbol{P})$ be the canonical variables in Cartesian coordinates. From $L = T - U = \frac{1}{2} m_n \left|\dot{\boldsymbol{Q}}\right|^2 - \left(U_B + U_g\right)$,

$$L = \frac{1}{2} m_n \left(\dot{X}^2 + \dot{Y}^2 + \dot{Z}^2\right) + |\boldsymbol{\mu}_n||\boldsymbol{B}| + m_n g Y \tag{3.18}$$

Then,

$$\boldsymbol{P} = \frac{\partial L}{\partial \dot{\boldsymbol{Q}}} = m_n\left(\dot{X}\widehat{\boldsymbol{X}} + \dot{Y}\widehat{\boldsymbol{Y}} + \dot{Z}\widehat{\boldsymbol{Z}}\right) = m_n\dot{\boldsymbol{Q}} \tag{3.19}$$

as there is no velocity dependence in either potential energy term. Following the derivation provided in Ref. [20], we perform a canonical transformation using the generating function of the third type, which depends on the old momentum $\boldsymbol{P}$ and new coordinate $\boldsymbol{r}$, as defined in Eq. (3.12):

$$F_3(\boldsymbol{P}; x, s, y) = F_3(\boldsymbol{P}, \boldsymbol{r}) = -\boldsymbol{P}\cdot\boldsymbol{r} \tag{3.20}$$

Thus, our new canonical momenta are

$$p_s = -\frac{\partial F_3}{\partial s} = \left(1 + \frac{x}{\rho}\right)\boldsymbol{P}\cdot\hat{\boldsymbol{s}} \tag{3.21a}$$

$$p_x = -\frac{\partial F_3}{\partial x} = \boldsymbol{P}\cdot\hat{\boldsymbol{x}} \tag{3.21b}$$

$$p_y = -\frac{\partial F_3}{\partial y} = \boldsymbol{P}\cdot\hat{\boldsymbol{y}} \tag{3.21c}$$

and the equations of motion in the new coordinate system are

$$\dot{s} = \frac{\partial H}{\partial p_s} \quad , \quad \dot{p}_s = -\frac{\partial H}{\partial s} \tag{3.22a}$$

$$\dot{x} = \frac{\partial H}{\partial p_x} \quad , \quad \dot{p}_x = -\frac{\partial H}{\partial x} \tag{3.22b}$$

$$\dot{y} = \frac{\partial H}{\partial p_y} \quad , \quad \dot{p}_y = -\frac{\partial H}{\partial y} \tag{3.22c}$$

3.2.3 Transverse motion

Although the present work concerns longitudinal synchrotron motion for neutrons, we make use of a few results from the extensive work done on transverse charged particle motion in accelerators. This description often begins with the model of a particle experiencing a force whose magnitude changes linearly with displacement from equilibrium, with the coefficient of proportionality being given the symbol K [20]; those familiar with the field will recognize this as the effect of quadrupole magnets on the transverse motion of charged particles. The mathematical description is the familiar homogeneous linear second-order differential equation of a simple harmonic oscillator:

$$x'' + Kx = 0 \tag{3.23}$$

When $K > 0$, it is called focusing; $K < 0$ is called defocusing ($K = 0$ is called drift space). However, the value of K changes as the particle travels through the accelerator: $K = K(s)$. When $K(s)$ is periodic, we get a form of Hill's equation [23]:

$$x'' + K(s)x = 0 \ , \quad K(s + L) = K(s) \tag{3.24}$$

where L is the period (i.e., length of the periodic structure in the accelerator).

The trivial solution of this equation—that is, $x = 0$ for all s—is called the closed orbit. The nontrivial solutions $x_\beta(s)$ constitute the so-called betatron oscillations, and betatron motion refers to the traverse motion of the particle around the closed orbit. However, the closed orbit is determined by a particle having the design momentum; off-momentum particles will follow a different trajectory through the system. As we will subsequently be using the language of energy rather than momentum, we will present the following formulation in terms of $\Delta E/E_0$ (where E_0 is the design energy and ΔE is the difference

between the particle's energy and the design energy), rather than the usual $\delta = \Delta p/p_0$ found in the literature on accelerator physics.

We now consider a linearized inhomogeneous off-energy Hill's equation, to lowest order in $\Delta E/E_0$ [20]:

$$x'' + K(s)x = \frac{1}{\rho} \tag{3.25}$$

The solution to this inhomogeneous equation is the linear superposition of the particular solution and the solution to the homogeneous equation, which we already found to be x_β. The particular solution, meanwhile, is $D(s)\frac{\Delta E}{E_0}$, yielding the full solution

$$x = x_\beta(s) + D(s)\frac{\Delta E}{E_0} \tag{3.26}$$

$D(s)$ is called the dispersion function. Although the present work will not require that we find an expression for it, we do make use of the fact that $D(s)\frac{\Delta E}{E_0}$ gives the off-energy closed orbit. We can therefore integrate over $D(s)$ to find the difference between the orbit path length of an off-energy particle and the design orbit:

$$\Delta C = \frac{\Delta E}{E_0}\oint \frac{D(s)ds}{\rho} \tag{3.27}$$

3.2.4 Synchronous particles

Before proceeding to develop longitudinal equations of motion, we must define the meaning of a synchronous particle. As is well known in the field, charged particle accelerators typically rely on cavities operating in the radio frequency (RF) range (from a few hundred kHz to 30

GHz in practice [20]) to accelerate particles. However, depending on the arrival time of the particle relative to the phase of the RF wave, the particle may lose energy to, rather than gain energy from, the longitudinal electric field. The effective gap voltage of the RF cavity at time t is given by a sinusoid:

$$\Delta V = V_0 \sin(\omega_{RF} t + \varphi_{RF}) \tag{3.28}$$

where V_0 is the maximum voltage, ω_{RF} is the frequency of operation, and φ_{RF} is the phase angle. A particle with charge e experiences a change in energy as it travels through the cavity gap equal to

$$\Delta E = e\Delta V = eV_0 \sin(\omega_{RF} t + \varphi_{RF}) \tag{3.29}$$

Hence, depending on the argument of the sinusoid, the change in energy per passage through the cavity may be positive or negative.

For circular accelerators, a particle will return to the cavity after one revolution. If the particle does so in such a manner that it always remains synchronized with the RF phase at revolution period T_0, it is called a synchronous particle. The angular revolution frequency of a synchronous particle is then

$$\omega_0 = \frac{2\pi}{T_0} \tag{3.30}$$

Note that ω_0 does not necessarily equal ω_{RF}: ω_{RF} may also be an integer multiple h of ω_0, that is,

$$\omega_{RF} = h\omega_0 \tag{3.31}$$

In this case, h is called the harmonic number.

3.2.5 Longitudinal equations of motion

We now begin the substance of the present work. We specify a B-field $\boldsymbol{B}$, in a region of length L, that changes only with spatial coordinate s and time t : $\boldsymbol{B} = B(s,t)$. If this B-field is generated by a sinusoidally time-varying current, such as that provided by an RF supply, the most general B-field can be written as a product of an amplitude function and a sine function, with both components possibly having s and t dependence:

$$B(s,t) = B_g(s,t)\sin[h\omega_0(s,t)t + \varphi_s] \tag{3.32}$$

Here, the subscript g is used to denote a gradient field amplitude, and φ_s is the phase angle for the synchronous particle with respect to the RF.

In practice, ω_0 cannot easily be made to vary with s, and varying ω_0 with t involves changes in energy and other engineering challenges for the RF supply. Therefore, we restrict the discussion on developing adiabatic capture to a fixed frequency, recognizing here that adiabatic capture can also be performed by varying other parameters. This simplification results in an s-dependence appearing only in the amplitude function $B_g(s,t)$, or

$$B(s,t) = B_g(s,t)\sin(h\omega_0 t + \varphi_s) \tag{3.33}$$

We further decompose $B_g(s,t)$ into separable components $C_g(s)$ and $I(t)$:

$$B_g(s,t) = C_g(s)I(t) \tag{3.34}$$

In other words, $I(t)$ is the field-generating alternating current amplitude, with only time dependence, and $C_g(s)$ is the proportionality constant for a given location s. For example, the B-field created by a so-called "window-frame dipole" [20] can be described by the equation

$$B = \mu_0 \frac{N}{g} I \tag{3.35}$$

where N is the number of coil turns, g is the gap length, and I is the current through each turn of coil. In this case, $C_g(s) = \mu_0 \frac{N}{g}$, with no explicit dependence on s. However, if the number of coils per unit gap can be made to vary with s, then $C_g(s) = \mu_0 \frac{N(s)}{g}$, etc.

For reasons that will become apparent shortly, we concern ourselves only with magnet geometries that create B-fields with a linear dependence on s. The details of such a magnet are beyond the scope of the present work; however, a possible design is mentioned in the discussion on practical considerations. Figure 3.3 shows what Eq. (3.34) would look like in such a case for differing values of $I(t)$ if $I(t)$ is constant during the passage, leaving $B_g(s,t)$ with only an explicit s dependence (we will return to this assumption shortly). Note that the field region L is magnetically insulated on both sides and that the neutron must exit the gradient field through a step-like transition, as required by the discussion in Section 3.1.

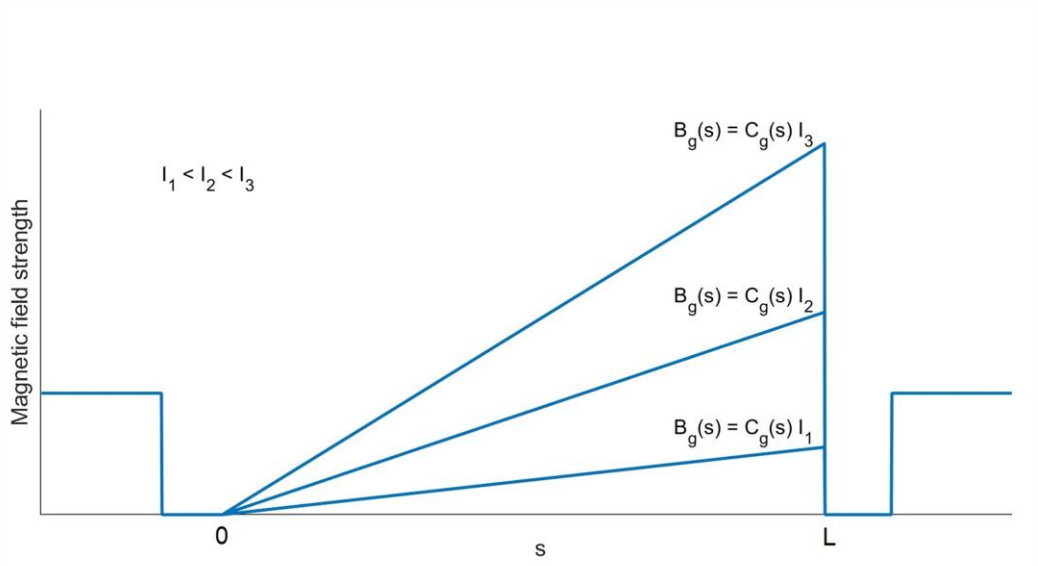

Figure 3.3: Linear ramping behavior through field region L when $I(t)$ takes different constant values during the neutron's passage through the alternating-current (AC) dipole magnet. Time-independent coefficient $C_g(s)$ is achieved geometrically. Magnetic insulation appears on both sides of the AC dipole.

With the assumption that $C_g(s)$ has a linear dependence on s, we can write

$$C_g(s) = C_g s \tag{3.36}$$

Then,

$$\frac{\partial C_g(s)}{\partial s} = C_g \tag{3.37}$$

and

$$\frac{\partial B_g(s,t)}{\partial s} = \frac{\partial}{\partial s} C_g(s) I(t) = C_g I(t) \tag{3.38}$$

Substituting Eq. (3.34) into Eq. (3.33) and using the result in Eq. (3.38), we have

$$B(s,t) = C_g(s) I(t) \sin(h\omega_0 t + \varphi_s) \tag{3.39}$$

$$\frac{\partial B(s,t)}{\partial s} = C_g I(t) \sin(h\omega_0 t + \varphi_s) \tag{3.40}$$

From Eq. (3.7), the change in energy of the neutron through the field region is

$$\Delta E = \int_{s_1}^{s_2} \frac{\partial}{\partial s} (-\boldsymbol{\mu} \cdot \boldsymbol{B})\, ds = \pm |\mu_n| \cos\theta \int_0^L \frac{\partial B(s,t)}{\partial s}\, ds \tag{3.41}$$

The upper sign corresponds to spin-up states, and the lower sign to spin-down states (recall from Section 2.2 that $\mu_n = -1.91304\, \mu_N$). The states will be either fully anti-aligned or aligned, respectively, so $\cos\theta = 1$. Substituting Eq. (3.40) in Eq. (3.41),

$$\Delta E = \pm |\mu_n| \int_0^L C_g I(t) \sin(h\omega_0 t + \varphi_s)\, ds \tag{3.42}$$

Let us now assume that $I(t)$ varies slowly, such that it can be considered constant during the passage of a neutron through the field region L. Then, $I(t)$ can be replaced by I_0, and we get

$$\Delta E = \pm|\mu_n|C_g I_0 \int_0^L \sin(h\omega_0 t + \varphi_s)\, ds \tag{3.43}$$

If the average velocity of the neutron through the field region with respect to s is v, then s is related to t via

$$s = vt \quad \rightarrow \quad ds = v\, dt \tag{3.44}$$

and we can rewrite Eq. (3.43) as

$$\Delta E = \pm|\mu_n|C_g I_0 v \int_0^{\frac{L}{v}} \sin(h\omega_0 t + \varphi_s)\, dt \tag{3.45}$$

This definite integral evaluates to

$$\Delta E = \mp|\mu_n|C_g I_0 \frac{v}{h\omega_0} \cos(h\omega_0 t + \varphi_s) \Big|_0^{\frac{L}{v}}$$

$$\Delta E = \mp|\mu_n|C_g I_0 \frac{v}{h\omega_0} \left[\cos\left(\frac{h\omega_0 L}{v} + \varphi_s\right) - \cos(\varphi_s)\right] \tag{3.46}$$

Using the trigonometric identities

$$\cos(\alpha + \beta) = \cos\alpha \cos\beta - \sin\alpha \sin\beta \tag{3.47a}$$

$$\cos(\alpha - \beta) = \cos\alpha \cos\beta + \sin\alpha \sin\beta \tag{3.47b}$$

with $\alpha = \varphi_s$ and $\beta = \frac{h\omega_0 L}{2v}$, we find (note the sign flip)

$$\Delta E = \mp|\mu_n|C_g I_0 \frac{v}{h\omega_0} \left[-2 \sin\left(\frac{h\omega_0 L}{2v}\right) \sin\varphi_s\right]$$

$$= \pm|\mu_n|C_g I_0 \frac{2v}{h\omega_0} \sin\left(\frac{h\omega_0 L}{2v}\right) \sin\varphi_s$$

$$= \pm|\mu_n|C_g I_0 \frac{2v}{h\omega_0} \left(\frac{L}{L}\right) \sin\left(\frac{h\omega_0 L}{2v}\right) \sin\varphi_s$$

$$\Delta E = \pm|\mu_n|B_g \sin\varphi_s \tag{3.48}$$

where

$$B_g = C_g I_0 L \frac{2v}{h\omega_0} \sin\left(\frac{h\omega_0 L}{2v}\right) \tag{3.49}$$

In other words, a synchronous neutron sees an effective field $B_g = C_g I_0 L \frac{2v}{h\omega_0} \sin\left(\frac{h\omega_0 L}{2v}\right)$ when passing through the field region L. Since this neutron has an angular revolution frequency of ω_0, it will encounter the field region L with a frequency of $f_0 = \frac{\omega_0}{2\pi}$ Hz. This results in a rate of energy change equivalent to

$$\frac{d}{dt}\Delta E = \dot{\Delta E} = \pm\frac{\omega_0}{2\pi}|\mu_n|B_g \sin\varphi_s \tag{3.50}$$

We now explore the behavior of non-synchronous neutrons in order to generate longitudinal equations of motion, following the traditional treatment used for circular charged particle accelerators and storage rings [20]. Non-synchronous neutrons can be described by their small deviations from the parameters of a synchronous neutron. Let ω_0 again be the synchronous revolution frequency and φ_s the RF phase angle for a synchronous neutron, as above. In addition, let θ_0 be the azimuthal orbital angle of a synchronous neutron through the storage ring and E_0 its energy. Then the equations describing the deviations of a non-synchronous neutron are

$$\omega = \omega_0 + \Delta\omega \tag{3.51a}$$

$$\varphi = \varphi_s + \Delta\varphi \tag{3.51b}$$

$$\theta = \theta_0 + \Delta\theta \tag{3.51c}$$

$$E = E_0 + \Delta E \tag{3.51d}$$

where the variables without subscripts will correspond to non-synchronous particles for the remainder of the discussion.

Since φ and $\Delta E/\omega_0$ can constitute a pair of conjugate phase-space coordinates, we find the time derivatives of these quantities in order to find equations of motion for the system. We start by noting that a change in the angular revolution frequency ω results from changes in the orbital angle with time, i.e., $\Delta\omega = \frac{d}{dt}\Delta\theta$. Meanwhile, there are h RF periods for every orbital period, and an advancing $\Delta\theta$ corresponds to a slipping $\Delta\varphi$ relative to the RF phase. Therefore,

$$\Delta\omega = \frac{d}{dt}\Delta\theta = -\frac{1}{h}\frac{d}{dt}\Delta\varphi = -\frac{1}{h}\frac{d}{dt}(\varphi - \varphi_s) = -\frac{1}{h}\frac{d\varphi}{dt} \tag{3.52}$$

since φ_s does not change with time. Rearranging this result and switching to dots for compactness, we have

$$\dot{\varphi} = -h\Delta\omega \tag{3.53}$$

However, we need to relate this result to our other phase-space coordinate, $\Delta E/\omega_0$, for it to be useful. To do this, we first establish a relationship with $\Delta E/E_0$, then proceed to create an equation of motion.

Let v_0 be the velocity and R_0 the average orbit radius of a synchronous neutron. Meanwhile, v and R will be the corresponding parameter for a non-synchronous neutron. The respective angular frequency will then be given identically by

$$\omega_0 = \frac{v_0}{R_0} \quad , \quad \omega = \frac{v}{R} \tag{3.54}$$

Combining these equations with Eq. (3.51a), we get

$$\frac{\Delta\omega}{\omega_0} = \frac{\omega - \omega_0}{\omega_0} = \frac{{}^{v}/_{R}}{{}^{v_0}/_{R_0}} - 1 = \frac{v}{v_0}\frac{R_0}{R} - 1 \tag{3.55}$$

Meanwhile, the kinetic energy of the synchronous and non-synchronous neutron, respectively, is

$$E_0 = \frac{1}{2}m{v_0}^2 \quad , \quad E = \frac{1}{2}mv^2 \tag{3.56}$$

since we are not in the relativistic regime. This yields, for the ratio of the velocities,

$$\frac{v}{v_0} = \frac{\sqrt{{}^{2E}/_{m}}}{\sqrt{{}^{2E_0}/_{m}}} = \sqrt{\frac{E}{E_0}} \tag{3.57}$$

Substituting this into Eq. (3.55), we get

$$\frac{\Delta\omega}{\omega_0} = \frac{v}{v_0}\frac{R_0}{R} - 1 = \sqrt{\frac{E}{E_0}}\left(\frac{R_0}{R}\right) - 1 = \sqrt{\frac{E_0 + \Delta E}{E_0}}\left(\frac{R_0}{R_0 + \Delta R}\right) - 1 \tag{3.58}$$

where we have applied Eq. (3.57) and likewise used the small-deviation formulation for R, i.e., $R = R_0 + \Delta R$. Invoking Eq. (3.27), which found the difference in orbit path length in terms of ΔE and E_0, ΔR is related to ΔE and E_0 via the integral

$$\Delta R = \frac{1}{2\pi}\frac{\Delta E}{E_0}\oint \frac{D(s)ds}{\rho} \tag{3.59}$$

We can write this more compactly as

$$\Delta R = \alpha_c R_0 \frac{\Delta E}{E_0} \tag{3.60}$$

$$\alpha_c \equiv \frac{1}{2\pi R_0}\oint \frac{D(s)ds}{\rho} \tag{3.61}$$

We call α_c the energy compaction factor due to its analog with the momentum compaction factor [20]. Substituting this definition of ΔR into Eq. (3.58), we get

$$\frac{\Delta\omega}{\omega_0} = \sqrt{\frac{E_0 + \Delta E}{E_0}}\left(\frac{R_0}{R_0 + \alpha_c R_0 \frac{\Delta E}{E_0}}\right) - 1$$

$$\frac{\Delta\omega}{\omega_0} = \sqrt{1 + \frac{\Delta E}{E_0}}\left(\frac{1}{1 + \alpha_c \frac{\Delta E}{E_0}}\right) - 1 \tag{3.62}$$

Expanding $\sqrt{1 + \Delta E/E_0}$ and $\frac{1}{1+\alpha_c \Delta E/E_0}$ in $\Delta E/E_0$, we get the following linearized equation for $\Delta\omega/\omega_0$ after all higher order terms of $\Delta E/E_0$ are disregarded:

$$\frac{\Delta\omega}{\omega_0} = \left[1 + \frac{1}{2}\frac{\Delta E}{E_0} - \frac{1}{8}\left(\frac{\Delta E}{E_0}\right)^2 + \cdots\right]\left[1 - \alpha_c \frac{\Delta E}{E_0} + \left(\alpha_c \frac{\Delta E}{E_0}\right)^2 - \cdots\right] - 1$$

$$\approx \left(1 + \frac{1}{2}\frac{\Delta E}{E_0}\right)\left(1 - \alpha_c \frac{\Delta E}{E_0}\right) - 1 = 1 + \frac{1}{2}\frac{\Delta E}{E_0} - \alpha_c \frac{\Delta E}{E_0} - \alpha_c \frac{1}{2}\left(\frac{\Delta E}{E_0}\right)^2 - 1$$

$$\frac{\Delta\omega}{\omega_0} \approx \frac{1}{2}\frac{\Delta E}{E_0} - \alpha_c \frac{\Delta E}{E_0} = \left(\frac{1}{2} - \alpha_c\right)\frac{\Delta E}{E_0} \tag{3.63}$$

In keeping with the convention of charged particle accelerators, we define a transition gamma γ_T such that

$$\gamma_T \equiv \sqrt{\frac{1}{\alpha_c}} \tag{3.64}$$

allowing us to write $\Delta\omega/\omega_0$ as

$$\frac{\Delta\omega}{\omega_0} = \left(\frac{1}{2} - \frac{1}{\gamma_T^2}\right)\frac{\Delta E}{E_0} = -\eta\frac{\Delta E}{E_0} \tag{3.65}$$

$$\eta = \left(\frac{1}{\gamma_T^2} - \frac{1}{2}\right) \tag{3.66}$$

Rearranging Eq. (3.65) to solve for $\Delta\omega$, we can now substitute it into Eq. (3.53) to get

$$\dot{\varphi} = -h\Delta\omega = h\omega_0\eta\frac{\Delta E}{E_0} = h\omega_0\eta\frac{\Delta E}{E_0}\left(\frac{\omega_0}{\omega_0}\right) \tag{3.67}$$

This results in our first longitudinal equation of motion:

$$\dot{\varphi} = \frac{h{\omega_0}^2\eta}{E_0}\left(\frac{\Delta E}{\omega_0}\right) \tag{3.68}$$

The second longitudinal equation of motion for our chosen pair of conjugate phase-space coordinates $(\varphi, \Delta E/\omega_0)$ requires that we find the time evolution of $\Delta E/\omega_0$ in terms of φ. We begin by applying the small-deviation formulation above to $1/\omega$, as well as to the product of $1/\omega$ and $\dot{E}$:

$$\frac{1}{\omega} = \frac{1}{\omega_0} + \Delta\left(\frac{1}{\omega}\right) \tag{3.69}$$

$$\frac{1}{\omega}\dot{E} = \frac{1}{\omega_0}\dot{E}_0 + \Delta\left(\frac{1}{\omega}\dot{E}\right) \quad \rightarrow \quad \Delta\left(\frac{1}{\omega}\dot{E}\right) = \frac{1}{\omega}\dot{E} - \frac{1}{\omega_0}\dot{E}_0 \tag{3.70}$$

Substituting Eq. (3.69) and the definition of $\dot{E} = \dot{E}_0 + \Delta\dot{E}$ into Eq. (3.70) yields

$$\begin{aligned}
\Delta\left(\frac{1}{\omega}\dot{E}\right) &= \left[\frac{1}{\omega_0} + \Delta\left(\frac{1}{\omega}\right)\right]\left(\dot{E}_0 + \Delta\dot{E}\right) - \frac{1}{\omega_0}\dot{E}_0 \\
&= \frac{1}{\omega_0}\dot{E}_0 + \frac{1}{\omega_0}\Delta\dot{E} + +\Delta\left(\frac{1}{\omega}\right)\dot{E}_0 + \Delta\left(\frac{1}{\omega}\right)\Delta\dot{E} - \frac{1}{\omega_0}\dot{E}_0 \\
&= \frac{1}{\omega_0}\Delta\dot{E} + +\Delta\left(\frac{1}{\omega}\right)\dot{E}_0 + \Delta\left(\frac{1}{\omega}\right)\Delta\dot{E}
\end{aligned}$$

$$\Delta\left(\frac{\dot{E}}{\omega}\right) \approx \frac{1}{\omega_0}\Delta\dot{E} + \Delta\left(\frac{1}{\omega}\right)\dot{E}_0 \tag{3.71}$$

because the Δ terms are defined as small deviations. This means that the linearized form of Eq. (3.70) is

$$\frac{1}{\omega}\dot{E} - \frac{1}{\omega_0}\dot{E}_0 \approx \frac{1}{\omega_0}\Delta\dot{E} + \Delta\left(\frac{1}{\omega}\right)\dot{E}_0 \tag{3.72}$$

Next, considering just $1/\omega$, its Taylor series expansion around the point E_0 is

$$\frac{1}{\omega} = \frac{1}{\omega_0} + \left[\frac{d\left(\frac{1}{\omega}\right)}{dE}\right]_0 (E - E_0) + \left[\frac{d^2\left(\frac{1}{\omega}\right)}{d^2E}\right]_0 \frac{(E - E_0)^2}{2} + \cdots \tag{3.73}$$

Per Eq. (3.51d), $E - E_0$ is equal to ΔE, while $1/\omega - 1/\omega_0$ is $\Delta(1/\omega)$. Therefore, after subtracting $1/\omega_0$ from both sides, we get

$$\Delta\left(\frac{1}{\omega}\right) = \left[\frac{d\left(\frac{1}{\omega}\right)}{dE}\right]_0 \Delta E + \left[\frac{d^2\left(\frac{1}{\omega}\right)}{d^2E}\right]_0 \frac{\Delta E^2}{2} + \cdots \approx \left[\frac{d\left(\frac{1}{\omega}\right)}{dE}\right]_0 \Delta E \tag{3.74}$$

As above, we have discarded terms above first order. Substituting this linear expression into Eq. (3.72) , we get

$$\frac{1}{\omega}\dot{E} - \frac{1}{\omega_0}\dot{E}_0 \approx \frac{1}{\omega_0}\Delta\dot{E} + \left(\left[\frac{d\left(\frac{1}{\omega}\right)}{dE}\right]_0 \Delta E\right)\dot{E}_0$$

$$= \frac{1}{\omega_0}\Delta\dot{E} + \Delta E\left[\frac{d\left(\frac{1}{\omega}\right)}{dE}\right]_0 \left(\frac{dE}{dt}\right)_0$$

$$= \frac{1}{\omega_0}\Delta\dot{E} + \Delta E\left[\frac{d\left(\frac{1}{\omega}\right)}{dt}\right]_0$$

$$\frac{1}{\omega}\dot{E} - \frac{1}{\omega_0}\dot{E}_0 = \frac{1}{\omega_0}\frac{d}{dt}\Delta E + \Delta E\frac{d}{dt}\left(\frac{1}{\omega_0}\right) \tag{3.75}$$

We recognize this last expression as an application of the product rule of differentiation:

$$\frac{1}{\omega_0}\frac{d}{dt}\Delta E + \Delta E\frac{d}{dt}\left(\frac{1}{\omega_0}\right) = \frac{d}{dt}\left(\Delta E\frac{1}{\omega_0}\right) \tag{3.76}$$

Therefore, the linearized relationship between the time evolution of the energy change and the RF phase angle φ of the non-synchronous neutron is

$$\frac{d}{dt}\left(\frac{\Delta E}{\omega_0}\right) = \frac{1}{\omega}\dot{E} - \frac{1}{\omega_0}\dot{E_0}$$

$$= \frac{1}{\omega}\left(\pm\frac{\omega}{2\pi}|\mu_n|B_g \sin\varphi\right) - \frac{1}{\omega_0}\left(\pm\frac{\omega_0}{2\pi}|\mu_n|B_g \sin\varphi_s\right)$$

$$= \pm\frac{1}{2\pi}|\mu_n|B_g(\sin\varphi - \sin\varphi_s)$$

We have thus found our second longitudinal equation of motion:

$$\frac{d}{dt}\left(\frac{\Delta E}{\omega_0}\right) = \pm\frac{1}{2\pi}|\mu_n|B_g(\sin\varphi - \sin\varphi_s) \tag{3.77}$$

As a reminder, our other longitudinal equation of motion is:

$$\dot{\varphi} = \frac{h{\omega_0}^2\eta}{E_0}\left(\frac{\Delta E}{\omega_0}\right)$$

These equations can alternatively be called synchrotron equations of motion and the motion they describe, "synchrotron motion".

A Hamiltonian H for phase-space coordinates $\left(\varphi, \frac{\Delta E}{\omega_0}\right)$, with time t as the independent variable, can be constructed by satisfying the Hamiltonian equations of motion:

$$\dot{\varphi} = \frac{\partial H}{\partial\left(\frac{\Delta E}{\omega_0}\right)} \quad , \quad \frac{d}{dt}\left(\frac{\Delta E}{\omega_0}\right) = -\frac{\partial H}{\partial\varphi} \tag{3.78}$$

From inspection, a possible Hamiltonian is then

$$H = \frac{h{\omega_0}^2\eta}{2E_0}\left(\frac{\Delta E}{\omega_0}\right)^2 \pm\frac{1}{2\pi}|\mu_n|B_g[\cos\varphi - \cos\varphi_s + (\varphi - \varphi_s)\sin\varphi_s] \tag{3.79}$$

4 ADIABATIC CAPTURE OF NEUTRONS

4.1 PHASE-SPACE MAPPING

Equations (3.68) and (3.77) describe the evolution of our longitudinal phase-space coordinates φ and $\Delta E/\omega_0$ in terms of time. We can reformulate this evolution in terms of the nth passage through the field region by noting that, in a lumped-element model in which the RF cavity generating the field is localized, each revolution with period $T = \frac{1}{f_0} = \frac{2\pi}{\omega_0}$ will correspond to one passage through the B-field. Thus, the derivative with respect to time is equivalent to the derivative with respect to passage number multiplied by $\frac{\omega_0}{2\pi}$, or

$$\frac{d}{dt} = \frac{\omega_0}{2\pi}\frac{d}{dn} \tag{4.1}$$

Applying this substitution to Eq. (3.77), we get

$$\frac{d}{dt}\left(\frac{\Delta E}{\omega_0}\right) = \frac{\omega_0}{2\pi}\frac{d}{dn}\left(\frac{\Delta E}{\omega_0}\right) = \pm\frac{1}{2\pi}|\mu_n|B_g(\sin\varphi - \sin\varphi_s)$$

$$\rightarrow \quad \frac{d}{dn}(\Delta E) = \pm|\mu_n|B_g(\sin\varphi - \sin\varphi_s) \tag{4.2}$$

where we have taken ω_0 out of the derivative because it is constant, and then simplified. Similarly, for Eq. (3.68), we get

$$\frac{d}{dt}(\varphi) = \frac{\omega_0}{2\pi}\frac{d}{dn}(\varphi) = \frac{h{\omega_0}^2\eta}{E_0}\left(\frac{\Delta E}{\omega_0}\right)$$

$$\rightarrow \quad \frac{d}{dn}(\varphi) = \frac{2\pi h\eta}{E_0}\Delta E \tag{4.3}$$

The evolution of the phase-space coordinates φ and $\Delta E/\omega_0$ can thus be tracked from the nth to the $(n+1)$th turn by applying the incremental changes above sequentially. That is, the mapping equations governing this turn-by-turn phase-space evolution are:

$$\Delta E_{n+1} = \Delta E_n \pm |\mu_n| B_g (\sin\varphi_n - \sin\varphi_s) \tag{4.4a}$$

$$\varphi_{n+1} = \varphi_n + \frac{2\pi h\eta}{E_0}\Delta E_{n+1} \tag{4.4b}$$

The Jacobian matrix of this mapping is

$$J = \frac{\partial(\Delta E_{n+1}, \varphi_{n+1})}{\partial(\Delta E_n, \varphi_n)} = \begin{bmatrix} \frac{\partial(\Delta E_{n+1})}{\partial(\Delta E_n)} & \frac{\partial(\Delta E_{n+1})}{\partial(\varphi_n)} \\ \frac{\partial(\varphi_{n+1})}{\partial(\Delta E_n)} & \frac{\partial(\varphi_{n+1})}{\partial(\varphi_n)} \end{bmatrix}$$

$$= \begin{bmatrix} \frac{\partial}{\partial(\Delta E_n)}\left[\Delta E_n \pm |\mu_n| B_g (\sin\varphi_n - \sin\varphi_s)\right] & \frac{\partial}{\partial(\varphi_n)}\left[\Delta E_n \pm |\mu_n| B_g (\sin\varphi_n - \sin\varphi_s)\right] \\ \frac{\partial}{\partial(\Delta E_n)}\left[\varphi_n + \frac{2\pi h\eta}{E_0}\Delta E_{n+1}\right] & \frac{\partial}{\partial(\varphi_n)}\left[\varphi_n + \frac{2\pi h\eta}{E_0}\Delta E_{n+1}\right] \end{bmatrix}$$

$$= \begin{bmatrix} 1 & \pm|\mu_n| B_g \cos\varphi_n \\ \frac{2\pi h\eta}{E_0}\frac{\partial(\Delta E_{n+1})}{\partial(\Delta E_n)} & \frac{\partial(\varphi_n)}{\partial(\varphi_n)} + \frac{2\pi h\eta}{E_0}\frac{\partial(\Delta E_{n+1})}{\partial(\varphi_n)} \end{bmatrix}$$

$$J = \begin{bmatrix} 1 & \pm|\mu_n| B_g \cos\varphi_n \\ \frac{2\pi h\eta}{E_0} & 1 \pm \frac{2\pi h\eta}{E_0}|\mu_n| B_g \cos\varphi_n \end{bmatrix} \tag{4.5}$$

where we note that $\frac{\partial(\Delta E_{n+1})}{\partial(\Delta E_n)}$ and $\frac{\partial(\Delta E_{n+1})}{\partial(\varphi_n)}$ are simply elements J_{11} and J_{12}, respectively. The determinant of this Jacobian matrix is

$$\begin{vmatrix} 1 & \pm|\mu_n| B_g \cos\varphi_n \\ \frac{2\pi h\eta}{E_0} & 1 \pm \frac{2\pi h\eta}{E_0}|\mu_n| B_g \cos\varphi_n \end{vmatrix}$$

$$= 1 \pm \frac{2\pi h\eta}{E_0}|\mu_n| B_g \cos\varphi_n - \left(\pm\frac{2\pi h\eta}{E_0}|\mu_n| B_g \cos\varphi_n\right) = 1$$

Since it is equal to 1 for a two-by-two Jacobian matrix, the mapping defined in Eqs. (4.4a) and (4.4b) satisfies the symplectic condition and preserves phase-space area [24].

4.2 ADIABATIC SYNCHROTRON MOTION

Equations (4.4a) and (4.4b) provide a method for determining neutron motion in our system that is separate from Hamiltonian formalism. The two approaches may yield different results. Agreement depends on whether or not the system Hamiltonian can be considered quasi-static during the time that the neutron energy is changing. In other words, if the change in energy of a neutron during each revolution is sufficiently small and η is sufficiently far away from 0, we can consider the mapping equations and Hamiltonian formalism equivalent. This regime is called adiabatic synchrotron motion [20]. Outside this regime, the Hamiltonian's dependence on time will need to be taken into account.

The standard condition for adiabatic synchrotron motion is [20]

$$\alpha_{ad} = \left|\frac{1}{\omega_s^2}\frac{d\omega_s}{dt}\right| = \frac{1}{2\pi}\left|\frac{dT_s}{dt}\right| \ll 1 \tag{4.6}$$

where ω_s is the so-called synchrotron frequency and T_s the synchrotron period. These quantities characterize particle orbits through longitudinal phase space. They generally differ from the corresponding quantity characterizing the neutron's physical orbit in the storage ring. The ratio between synchrotron frequency and physical angular revolution frequency is known as the synchrotron tune Q_s:

$$Q_s = \frac{\omega_s}{\omega_0} = \frac{T_0}{T_s} \tag{4.7}$$

Reference [20] provides the value $\alpha_{ad} \leq 0.05$ as a good rule of thumb based on the experience of accelerator physicists working with charged particle accelerators.

4.3 SIMULATION RESULTS

The simulations that follow were all performed using custom MATLAB code implementing mapping equations Eqs. (4.4a) and (4.4b) to generate phase-space plots. For simulations presented in Sections 4.3.1 through 4.3.6, Table 4.1 lists the fixed values used for parameters. These values were chosen based on physical plausibility and expected efficacy in the simulations. Specifically, 1-Telsa fields are very achievable without superconducting technology, and a 1-Hertz revolution frequency for neutrons with kinetic energies around 1 μeV (i.e., velocities around 13.865 m/s) results in a ring about 4.4 m in diameter. Simulations

Parameter	Value
Average kinetic energy	$E = 1\ \mu eV$
Maximum B-field	$B_{g,max} = 1\ T$
Synchronous revolution frequency	$f_0 = 1\ Hz$
Harmonic number	$h = 1$
Synchronous phase	$\varphi_s = 0$
Slip factor	$\eta = -\frac{1}{2}$

Table 4.1: Simulation parameters for Sections 4.3.1 through 4.3.5

presented in Sections 4.3.7, 4.3.8, and 4.4 will have had their parameters varied as noted in the text.

As covered in Chapter 2, the neutron possesses two spin states: up and down, with the spin-up state corresponding to a negative value for μ_n. The negative value for μ_n is used explicitly in the code, so spin-up neutrons are used implicitly in the simulations. However, switching the polarity of the magnet will negate a change in sign of μ_n, as would occur with the use of spin-down neutrons. Therefore, the results that follow are valid for both spin-up and spin-down neutrons so long as the magnet polarity is properly configured.

4.3.1 Phase-space ellipses

To confirm the expected steady-state behavior of the mapping equations, the non-ramping condition with on-energy neutrons was simulated. Particles circulating in a storage ring in the absence of changing magnetic conditions should exhibit simple harmonic motion and trace out constant phase-space ellipses [20]. Figure 4.1 shows these ellipses for 200 iterations of the mapping equations, which is equivalent to each neutron undergoing 200 turns through the ring and thus 200 passages through the field region, with B_g held at 1 T. The baseline behavior of the mapping equations was therefore as expected.

4.3.2 Synchrotron tune

As a second check on the expected simple harmonic motion in steady-state conditions, we look at synchrotron tune versus phase. As seen in Eq. (4.7), the synchrotron tune is a measure

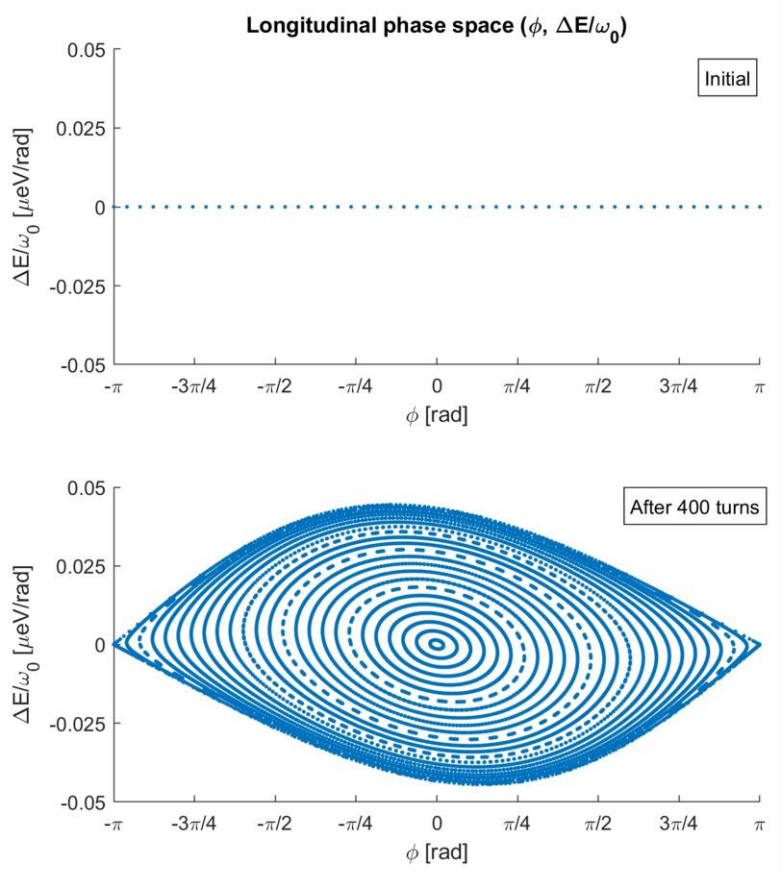

Figure 4.1: Longitudinal phase-space mapping equations applied in steady-state conditions. On-energy neutrons trace out constant phase-space ellipses, as expected. Since $h = 1$, the phase of the entire ring goes from $-\pi$ to π.

of a neutron's period in the physical system (orbital period) compared to its period in phase space, where it is tracing out a constant phase-space ellipse. Figures 4.2(a)-(c) show the steps for generating the desired curve. First, the phase of each on-energy neutron in Fig. 4.1 is plotted versus turn number, as shown in Fig. 4.2(a). Then, a fast Fourier transform is performed on the resulting sinusoidal curves, and the tune corresponding to the peak of the FFT spectrum is assigned as that neutron's tune, as shown in Fig. 4.2(b). The tune is then

plotted versus the neutron's initial on-energy phase, furnishing Fig. 4.2(c). This is the expected relationship [20].

The turn-by-turn change in the synchrotron tune provides us with another definition of the adiabatic condition. From Eq. (4.6), one version of the adiabatic condition is

$$\alpha_{ad} = \left| \frac{1}{\omega_s^2} \frac{d\omega_s}{dt} \right| \ll 1$$

The ratio ω_s/ω_0, in addition to being the definition of the synchrotron tune Q_s, is related to the synchrotron tune of the "stationary bucket" ν_s via

$$\frac{\omega_s}{\omega_0} = \nu_s \sqrt{|\cos \varphi_s|} \tag{4.8}$$

In this case, since we are examining the synchronous phase, $\varphi_s = 0$ and

$$\omega_s = \nu_s \omega_0 \tag{4.9}$$

Substituting,

$$\alpha_{ad} = \left| \frac{1}{\omega_s^2} \frac{d\omega_s}{dt} \right| = \left| \frac{1}{\nu_s^2 \omega_0^2} \frac{d}{dt} (\nu_s \omega_0) \right| = \left| \frac{1}{\nu_s^2 \omega_0^2} \left(\omega_0 \frac{d\nu_s}{dt} \right) \right| \tag{4.10}$$

Equation (4.1) provides our conversion of dt to dn, or $dt = 2\pi dn/\omega_0$. Substituting for dt and then replacing the differentials with discrete changes,

$$\alpha_{ad} = \left| \frac{1}{\nu_s^2 \omega_0^2} \left(\omega_0 \frac{d\nu_s}{2\pi dn / \omega_0} \right) \right| = \left| \frac{1}{2\pi \nu_s^2} \left(\frac{\Delta \nu_s}{\Delta n} \right) \right| \tag{4.11}$$

This provides a numerical check during simulations. Alternatively, applying the analysis done with charged particles circulating in a storage ring [20],

$$\Delta \nu_s = \sqrt{\frac{h \eta \Delta E}{4\pi E_0}} \tag{4.12}$$

where ΔE is the change in the neutron's energy for a given turn, i.e., $\Delta E = |\mu_n| B_g$. Adiabaticity can therefore be improved by changing B_g more smoothly turn by turn.

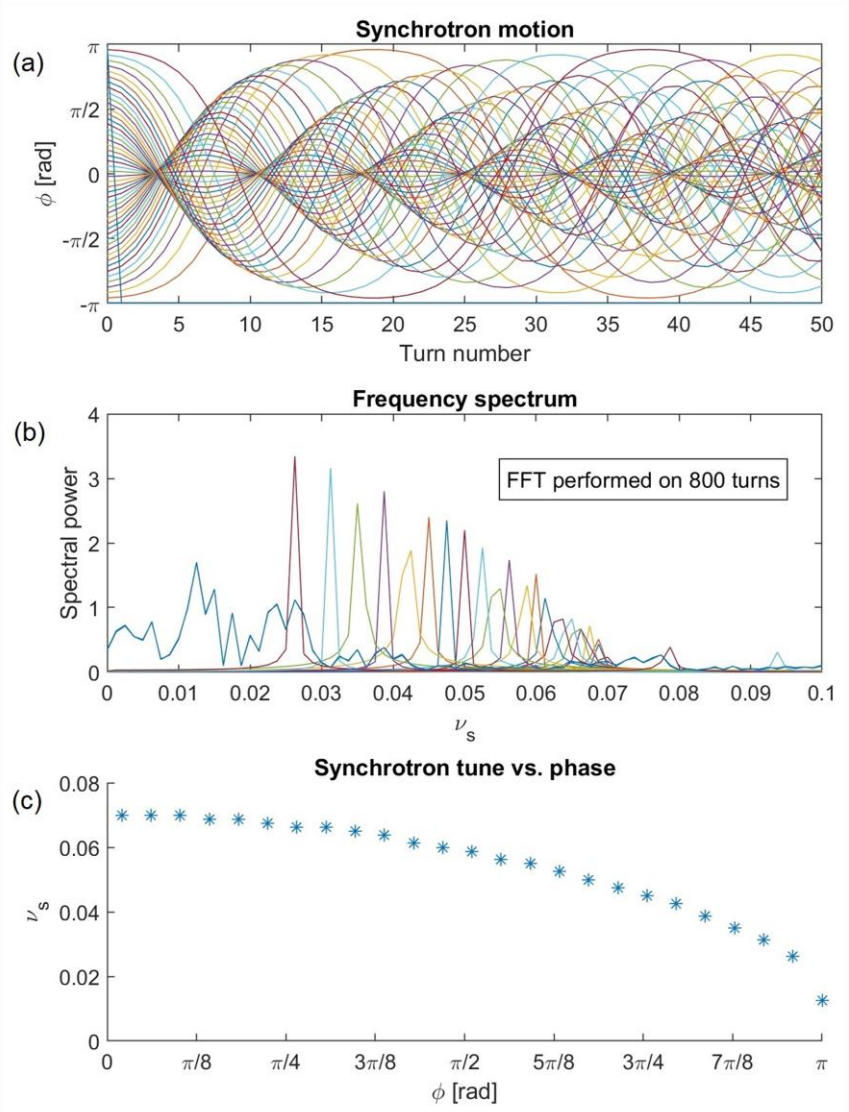

Figure 4.2: Synchrotron tune versus phase in steady-state conditions. (a) The phases of on-energy neutrons are plotted versus turn number. (b) A fast Fourier transform is performed on the curves in (a). The tune corresponding to the peak is assigned to that neutron's initial phase. (c) Tune is plotted versus phase, showing the relationship expected of a simple harmonic oscillator.

4.3.3 Maxwellian energy distribution

At first, adiabatic capture was attempted with a continuous beam exhibiting a Maxwellian energy distribution, which is the energy distribution of thermalized neutrons, as covered in Section 2.1. Through repeated elastic collisions with nuclei of the moderator, these neutrons reach thermal equilibrium and have an energy proportional to temperature:

$$E = \frac{1}{2}mv^2 = kT \tag{4.13}$$

where $k = 1.38 \times 10^{-23}\ J/K$ is the Boltzmann constant. The resulting fluxes (neutrons per unit area per second at energy E), confirmed experimentally [1], follow the distribution

$$\varphi_T = \frac{\varphi_0}{(kT)^2} E e^{-\frac{E}{kT}} \tag{4.14}$$

Accordingly, kT is the most probable energy (peak of the relative flux curve), and it is this value that is set to the nominal neutron energy of 1 μeV. The integration of φ_T over E yields the neutron current (neutrons per second).

The method used for initializing a randomized continuous neutron beam is as follows: a neutron is first sampled from the specified energy distribution and then randomly placed in phase according to the uniform distribution. The process is repeated until the neutron beam consists of the total number of neutrons needed for the simulation. In this case, the prescribed energy distribution is Maxwellian, although the actual code used a Gamma distribution random number generator in the absence of a dedicated Maxwell distribution random number generator (see the Appendix for how to achieve equivalency). Figure 4.3 shows a result of this process, with the histogram of neutron energies clearly exhibiting the expected Maxwellian shape and a peak around 1 μeV.

Adiabatic capture was then attempted using a linear ramp to the maximum B-field. Owing to the prevailing neutron lifetime value of about 878 seconds [25], the code's N_{ramp} parameter—which dictates how many turns it takes for the magnet to reach the maximum B-field strength—would need to be as small as possible to extend the useful experimentation time with the final neutrons. On the other hand, the ramp could not be too fast and violate the adiabaticity condition; furthermore, a more adiabatic capture leads to better phase space density at the end of the process [20]. An N_{ramp} value of 200 turns ($\Delta B_g = 0.005\,T$) was therefore taken as a good starting point for simulations. However, as shown in the corresponding results in Fig. 4.4, no discernible bunching was seen in the beam. Different ramp slopes up to $N_{ramp} = 800$ were subsequently tried in case the analytical adiabatic condition was invalid somehow, but the results remained substantially unchanged. Finally, the maximum B-field $B_{g,max}$ was even increased to as much as 5 T to investigate the feeble response in the beam, but still no overall bunching was observed. At this point, it became clear that an initial continuous Maxwellian beam would essentially remain a continuous Maxwellian beam, as it could not be meaningfully bunched in this manner due to excessive energy spread.

From this finding, it was concluded that a more monochromatic initial neutron beam would be needed for successful adiabatic capture with a ramping dipole magnetic field. However, since neutron transport lines generally involve bends and other structures that perform energy filtering as a matter of course—and the storage ring itself would impose an energy acceptance by virtue of its lattice and physical attributes—this was not a problematic result. The investigation therefore turned to exploring the theoretical limits and efficiency of adiabatic capture.

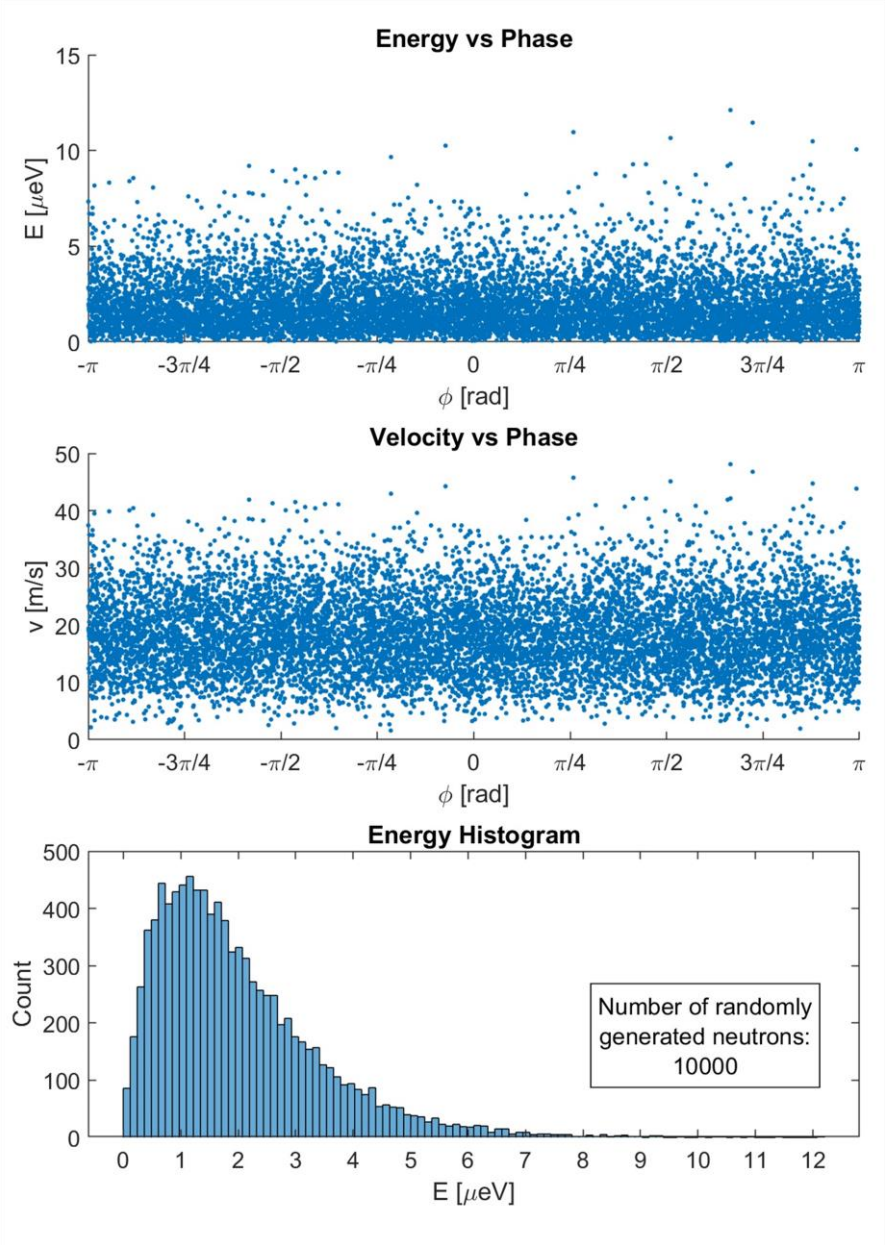

Figure 4.3: Randomized continuous neutron beam exhibiting a Maxwellian energy distribution. Neutrons are first sampled in energy, then placed randomly in phase according to the uniform distribution. Velocity is calculated from the relationship $\frac{1}{2}mv^2 = kT$ governing thermalized neutrons.

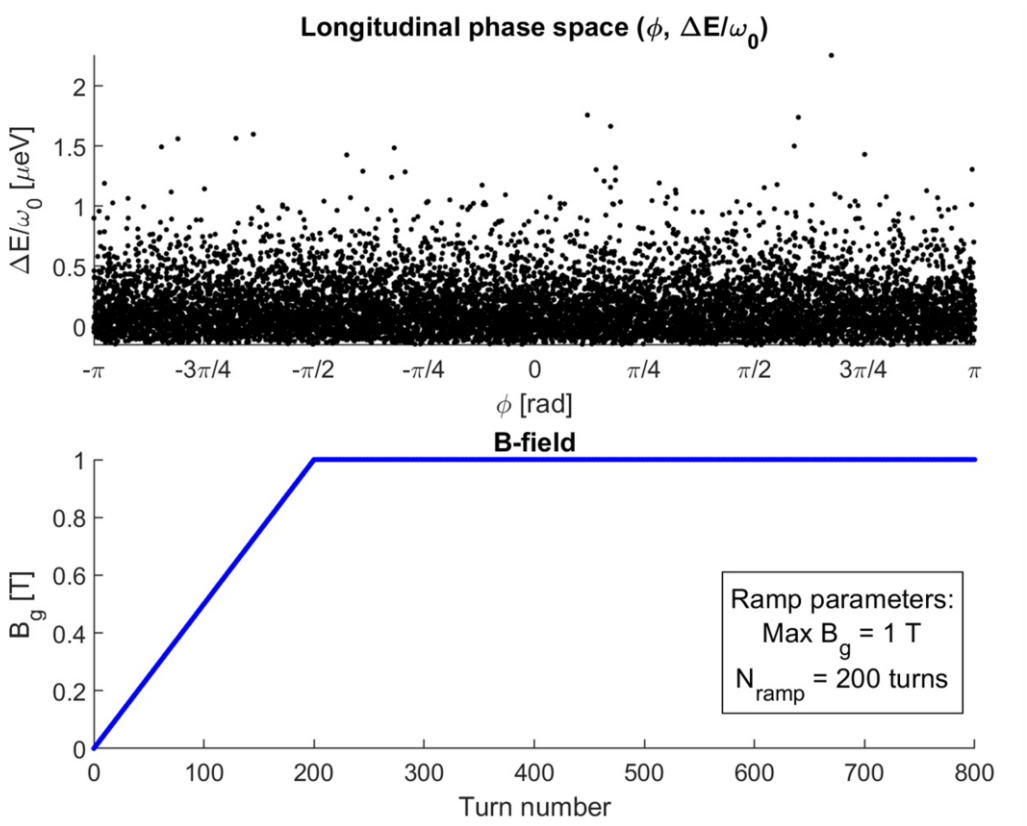

Figure 4.4: Negative simulation results with a continuous Maxwellian beam. The bottom plot shows the magnet ramp used to attempt adiabatic capture. The top plot is the neutron beam in longitudinal phase space at the end of the ramp.

4.3.4 Adiabatic capture and ramp functions

In Section 4.3.1, the phase-space analysis was performed with on-energy neutrons ($\Delta E = 0$) uniformly distributed in phase and circulating around the ring while B_g remained constant. To characterize the quality of the adiabatic capture, a similar method was used, but with B_g now allowed to ramp. Furthermore, in addition to on-energy neutrons, neutrons at different

levels of $\Delta E/E_0$ were sent through the system. The plots on the left of Fig. 4.5 show the results for $\Delta E/E_0 = 0.0, 0.025, 0.05, 0.1, 0.15$, and 0.2 when using the linear ramp from the previous subsection. The number of neutrons participating in the simulation was 10,000.

In comparing the topmost left plot in Fig. 4.5 with the bottom plot in Fig. 4.1, the beam has clearly been bunched in longitudinal phase space for on-energy neutrons. The remaining plots on the left show successful adiabatic capture until somewhere between $\Delta E/E_0 = 0.15$ and $\Delta E/E_0 = 0.2$. Although this was a good result, there was reason to believe that a smoother ramp function, such as one based on the hyperbolic tangent (tanh) function, would result in better bunching and hence lower emittance in the final beam [26]; in fact, a real magnet ramp would more closely resemble a tanh function than a simple piecewise linear function, which has nondifferentiable endpoints. Consequently, the plots on the right of Fig. 4.5 show the simulations all repeated using the ramp shown in the bottom righthand plot. In the code, this magnetic field is given by

$$B_g = \frac{1}{2} B_{g,max} \left[\tanh\left(slope\_factor \times \frac{n + offset - N_{ramp}}{N_{ramp}/2} \right) + 1 \right] \tag{4.15}$$

where $slope\_factor$ governs the steepness of the ramp, $offset$ horizontally translates the ramp, N_{ramp} is the characteristic duration of the ramp in turns, and n is the turn number. The values chosen ($slope_{factor} = 2$ and $offset = 0$) were manually optimized.

While the two ramps lead to very similar behavior for $\Delta E/E_0$ far from zero, there is a significant difference in the area and filamentation of the final phase-space ellipse for $\Delta E/E_0$ closer to zero, and the effect is most pronounced for the on-energy neutrons. This indicates that the dynamic aperture is largely determined by the bucket height set by $B_{g,max}$, while phase-space mixing and emittance are driven by the ramp. Due to the better bunching and more realistic ramping, a tanh function was used for the remaining work.

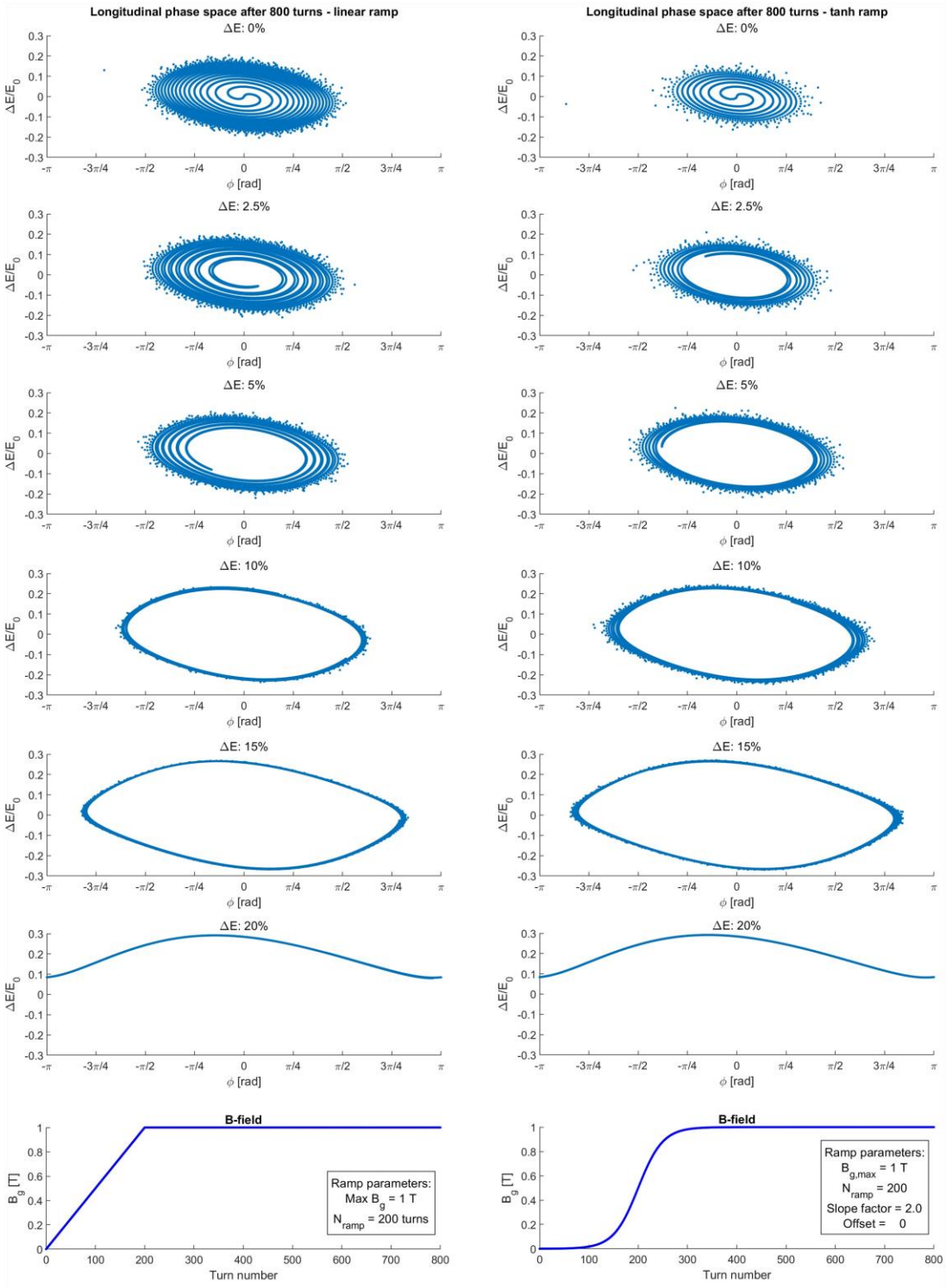

Figure 4.5: Comparison of adiabatic capture using a linear ramp (left plots) and a tanh-function ramp (right plots).

4.3.5 Analytical bucket

A noticeable feature in the plots of the longitudinal phase space of the beams that have undergone adiabatic capture is that their bucket is tilted and asymmetrical. We can compare it to the theoretical bucket by calculating the analytical Hamiltonian contour. From Eq. (4.79), the Hamiltonian for our system is given by

$$H = \frac{h{\omega_0}^2\eta}{2E_0}\left(\frac{\Delta E}{\omega_0}\right)^2 \pm \frac{1}{2\pi}|\mu_n|B_g[\cos\varphi - \cos\varphi_s + (\varphi - \varphi_s)\sin\varphi_s]$$

The separatrix defines the boundary between stable and unstable trajectories in phase space and corresponds to what is called the RF bucket in charged-particle accelerators; however, this work will drop "RF" because the frequencies involved are much lower than RF frequencies. The unstable fixed points occurring at $\Delta E = 0$ and $\varphi = \pi$ or $\varphi = -\pi$ are used for finding the separatrix [20]. With $\varphi_s = 0$, we get

$$H_{sx} = \pm\frac{1}{2\pi}|\mu_n|B_g(-2) \tag{4.16}$$

Setting H_{sx} equal to H (with φ_s again equal to zero),

$$\frac{h{\omega_0}^2\eta}{2E_0}\left(\frac{\Delta E}{\omega_0}\right)^2 \pm \frac{1}{2\pi}|\mu_n|B_g(\cos\varphi - 1) = \pm\frac{1}{2\pi}|\mu_n|B_g(-2)$$

$$\frac{h\eta}{2E_0}(\Delta E)^2 = \pm\frac{1}{2\pi}|\mu_n|B_g(-1 - \cos\varphi)$$

$$\Delta E = \pm\sqrt{\frac{E_0|\mu_n|B_g(-1-\cos\varphi)}{\pi h\eta}} \tag{4.17}$$

Note that we have eliminated the sign governing spin-up versus spin-down neutrons by assuming that the polarity of B_g is always correctly matched to the spin state, thereby

resulting in an overall positive value. However, since ΔE is squared, the value after the square root can be either positive or negative, constituting the upper half and bottom half of the separatrix, respectively. When plotted against φ, Eq. (4.17) gives the analytical bucket.

Figure 4.6 shows the evolution of this analytical bucket as the field ramps up during adiabatic capture. Lines of constant initial $\Delta E/E_0$, spaced by $\Delta E/E_0 = 0.025$ and color-coded, are also plotted; each initial line consists of 1000 neutrons. A closeup of the bottom right plots, which display the final bucket and phase-space distribution after 800 turns, along with the field value with turn number, is shown in Fig. 4.7. The deviations of the numerical bucket from the analytical bucket can be attributed to the Hamiltonian not taking nonlinearities (resonances) into account.

4.3.6 Numerical dynamic aperture

Lines of constant initial $\Delta E/E_0$ can be used to determine numerically the dynamic aperture of the adiabatic capture. By decreasing the spacing between the energy levels and increasing the number of neutrons per level, we can increase the resolution of the result, albeit at the expense of computation. This approach was done with 200 pairs of off-energy levels separated by $\Delta E/E_0 = 0.001$, for an analysis from -20% to $+20\%$. Each level was initially populated with 5000 neutrons. Figure 4.8(a) shows the initial and final phase space. The uncaptured lines in Fig. 4.8(b) can be counted and, together with the initial off-energy range and level spacing, used to determine the maximum off-energy level captured. There are 25 lines counting from both the bottom and the top; line 26 on both sides is fully captured. Thus, from the abrupt transition demarcating the separatrix, the simulation reveals 100% capture efficiency for $\pm 17.4\%$ $\Delta E/E_0$, with a resolution of 0.1%.

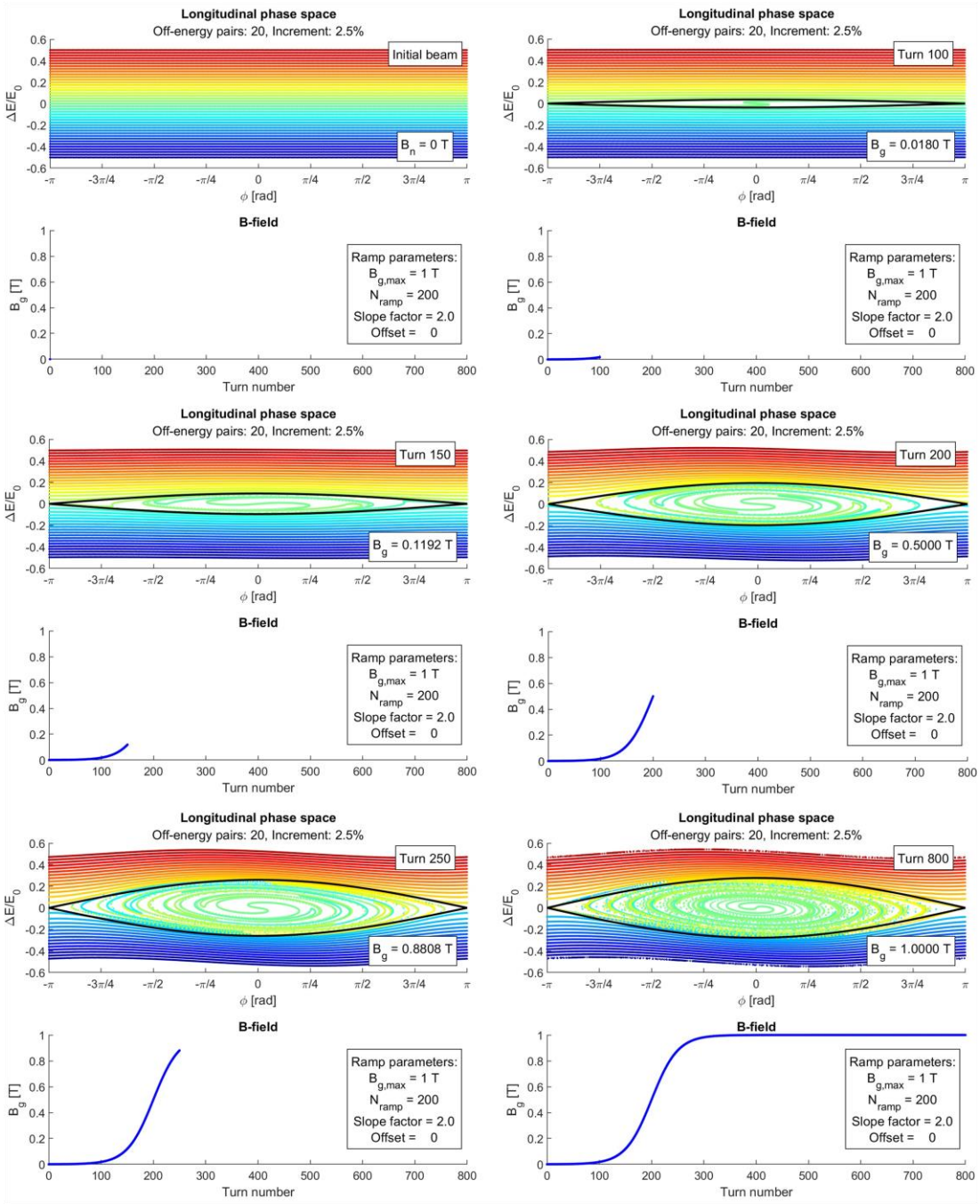

Figure 4.6: Evolution of the analytical bucket and lines of constant initial $\Delta E/E_0$ with ramping field. Each initial line comprises 1000 neutrons, and the lines are spaced by $\Delta E/E_0 = 0.025$.

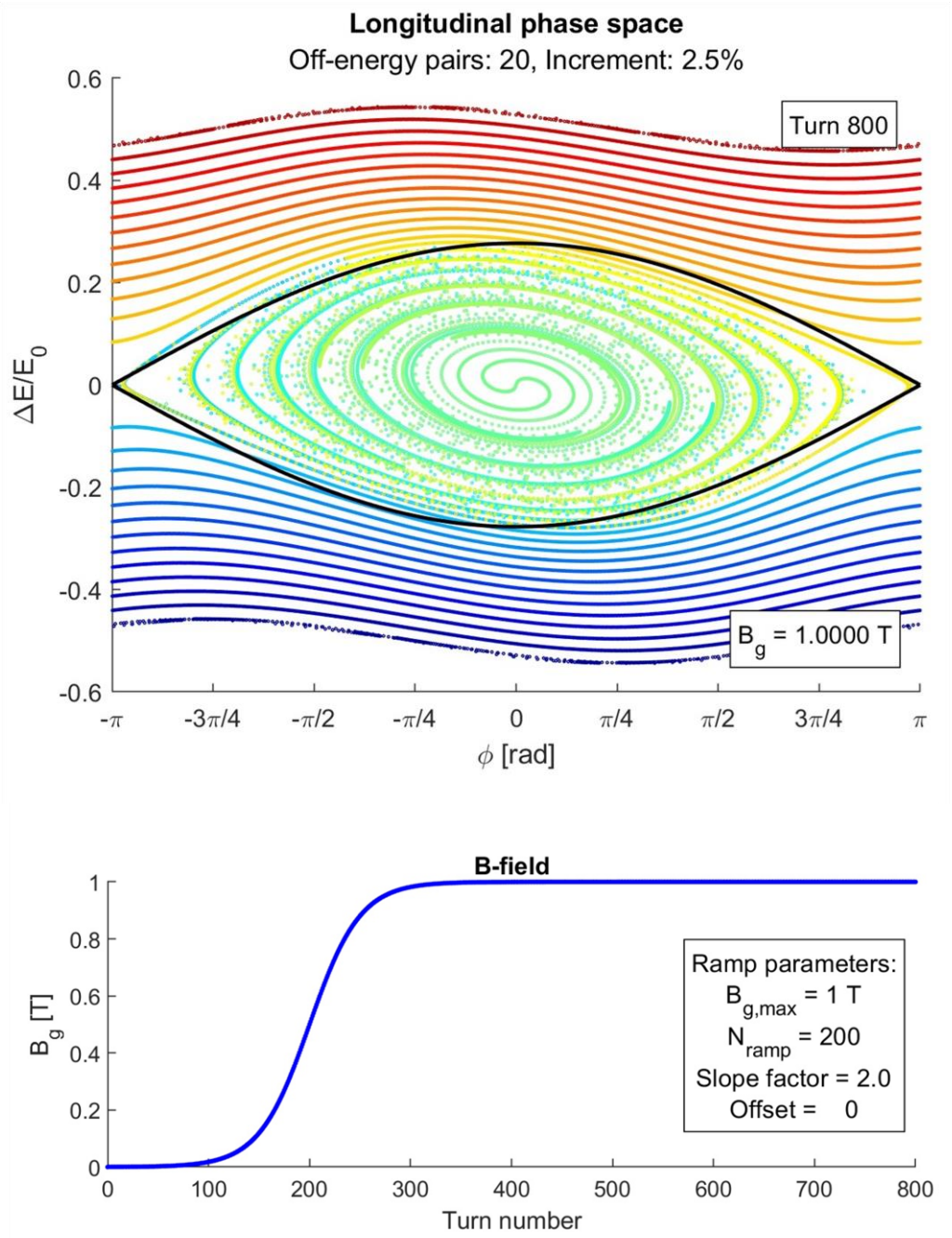

Figure 4.7: Evolution of the analytical bucket and lines of constant initial $\Delta E/E_0$. Each initial line comprised 1000 neutrons, and the lines were spaced by $\Delta E/E_0 = 0.025$.

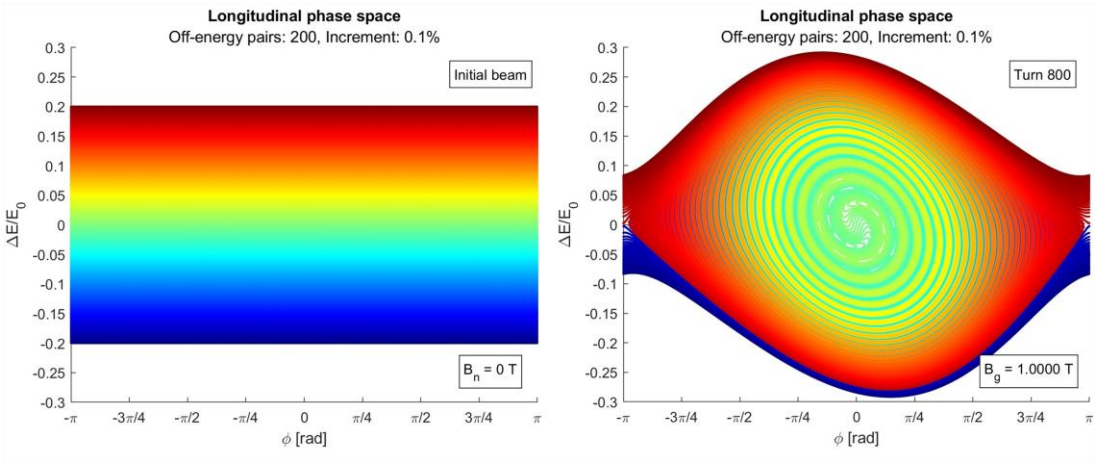

(a)

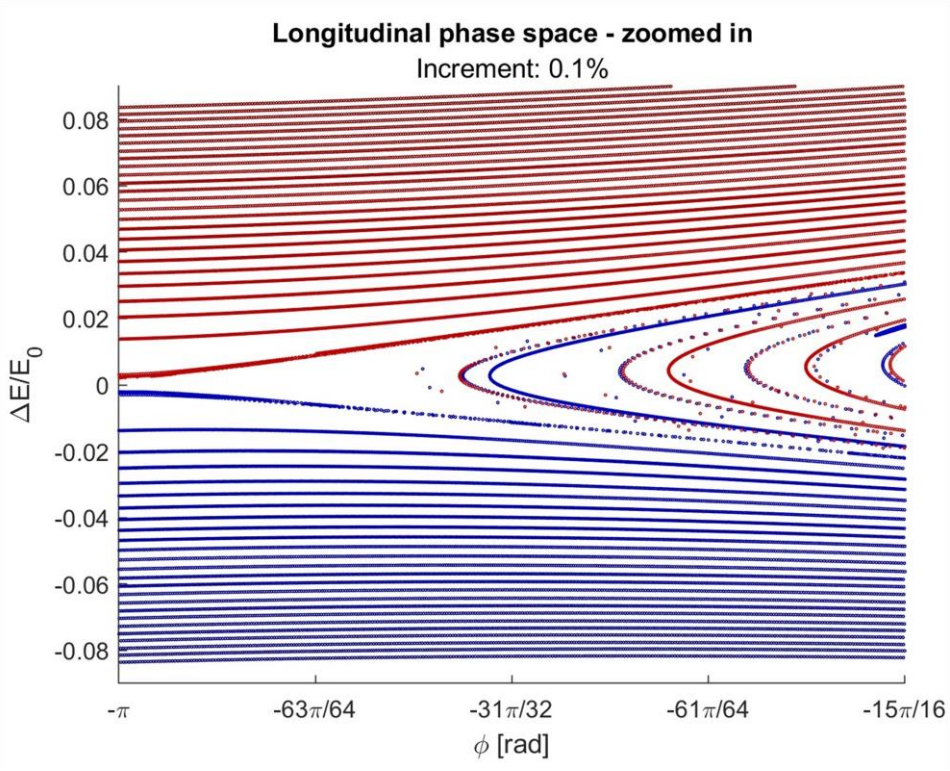

(b)

Figure 4.8: Numerical determination of the dynamic aperture. Plot (b) is a closeup of the left edge of the right plot in (a) and shows 25 uncaptured lines counting from both the bottom and the top after the simulation is complete. Line 26 on both sides is fully captured. Since the initial off-energy range was $\pm 20\%$ and the level spacing 0.1%, the dynamic aperture is $\pm 17.4\%$.

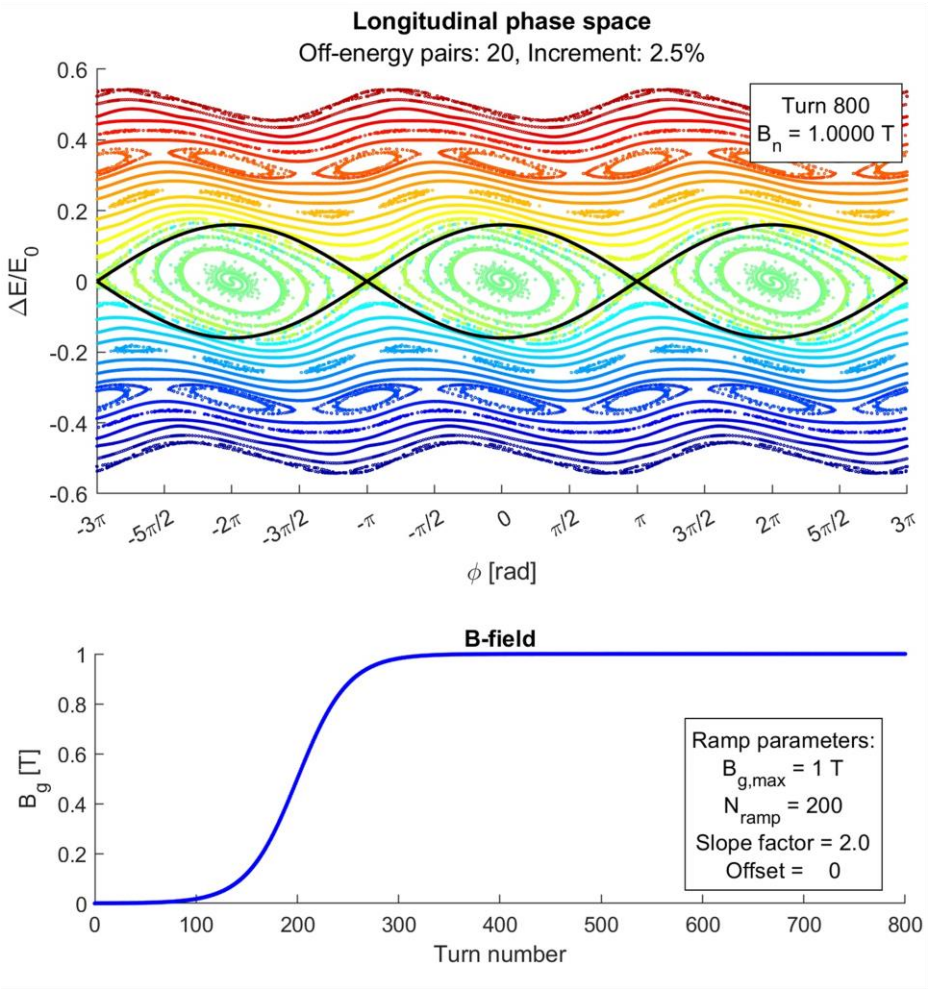

Figure 4.9: Adiabatic capture with $h = 3$

4.3.7 Higher harmonics

Although a study of higher harmonics is beyond the scope of the present work, the simulation code permits them. Figure 4.9 shows the result of repeating the simulation performed in Section 4.3.5 but with $h = 3$. The phase-space structure clearly shows that neutron storage rings are subject to the same considerations regarding resonances and other dynamics as charged-particle storage rings.

4.3.8 Other findings

Lastly, as a curiosity, if the polarity of the ramping magnet happens to be backwards for the spin state, the simulations show that, all else being equal through the ring, the preceding results are simply shifted by π. See Fig. 4.10. Of course, since spin-up and spin-down neutrons bend in opposite directions, if the ring magnets are likewise backwards, the neutrons will bend out of orbit after passing through the ramping magnet.

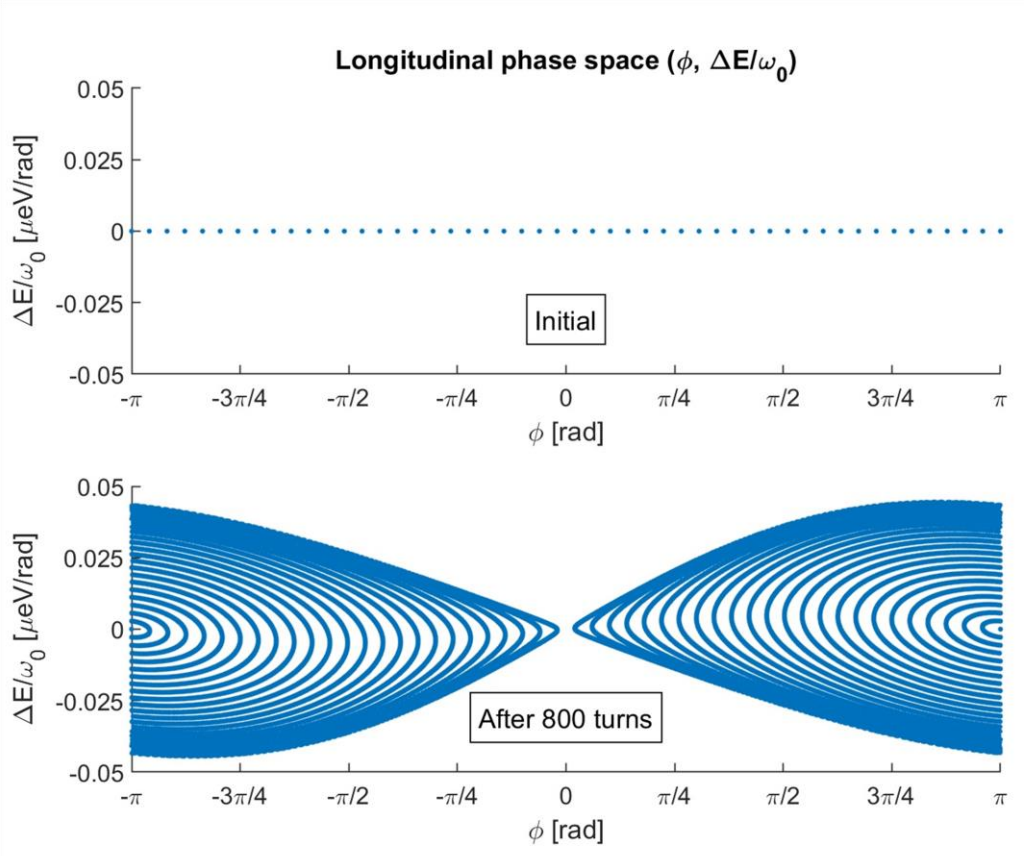

Figure 4.10: π phase slippage with backwards magnet polarity. However, results are otherwise identical.

4.4 OPTIMIZATION

As stated previously, the parameter values specifying the tanh ramp function used in the simulations of Sections 4.3.4 through 4.3.8 were selected via manual optimization. It is reasonable to assume that these values can be improved further by numerical methods. The following subsections report some results from a few investigations into the optimization space.

4.4.1 Global bunch length minimum via evolutionary algorithms

Given the present work's focus on spatially localizing neutrons as much as possible, bunch length following adiabatic capture was a natural value to try to minimize since, for a fixed number of neutrons in a bunch, a shorter bunch length entails a greater average neutron density within the bunch. Although phase-space area (emittance) is traditionally considered the relevant figure of merit in accelerator physics [20], for the purposes of the following optimization problems, energy spread will be considered secondary to phase—and hence spatial—spread. The objective function for minimization will then solely reflect the neutron bunch's extent in phase, with energy information projected onto the phase axis.

The comparison between the linear ramp and the tanh ramp in Section 4.3.4 indicated that neutrons initially on or near design energy responded most sensitively to the differences in the ramps, whereas neutrons initially more significantly off energy (i.e., $\Delta E/E_0 > \pm 10\%$) exhibited final phase-space trajectories that were essentially identical in both cases, being largely determined by the final stationary bucket after ramping. We will therefore use the

bunch length of the most sensitive case, $\Delta E/E_0 = 0$, as a proxy for the quality of the adiabatic capture: the smaller the final on-energy bunch length, the more effective the bunching and the less phase-space mixing in the final distribution.

As a slight complication, the phase-space ellipse of on-energy neutrons undergoes the most rotation due to nonlinearities, as seen in the top plots of Fig. 4.5. A root-mean-square (RMS) fit to the final bunch in phase space will therefore need to involve a rotated ellipse. Beginning with the standard equation for an unrotated ellipse,

$$\frac{x'^2}{a^2} + \frac{y'^2}{b^2} = 1 \tag{4.18}$$

and noting that the smallest angle of rotation ψ in this case occurs in the clockwise direction, we apply the rotation matrix

$$R_{cw} = \begin{pmatrix} \cos\psi & \sin\psi \\ -\sin\psi & \cos\psi \end{pmatrix} \tag{4.19}$$

to coordinates X and Y in the unrotated frame to yield the necessary transformation:

$$\begin{pmatrix} x' \\ y' \end{pmatrix} = \begin{pmatrix} \cos\psi & \sin\psi \\ -\sin\psi & \cos\psi \end{pmatrix} \begin{pmatrix} X \\ Y \end{pmatrix} \tag{4.20}$$

$$x' = X\cos\psi + Y\sin\psi \tag{4.21a}$$

$$y' = Y\cos\psi - X\sin\psi \tag{4.21b}$$

For our coordinate system in phase space, the X-axis in these equations corresponds to φ and the Y-axis corresponds to $\Delta E/E_0$. This gives, for the equation of the fitted phase-space ellipse,

$$\frac{\left(\varphi\cos\psi + \frac{\Delta E}{E_0}\sin\psi\right)^2}{a^2} + \frac{\left(\frac{\Delta E}{E_0}\cos\psi - \varphi\sin\psi\right)^2}{b^2} = 1 \tag{4.22}$$

There are therefore three parameters to be determined in this nonlinear data-fitting problem: a, b, and ψ. Note that the on-energy neutrons initially at $\varphi = \pm\pi$ will be ignored in the fit since, in the absence of numerical errors, these would be fixed stable points, rather than part of the bucket. To mitigate the effect of noise further, 10,000 neutrons are used.

As with the search and evolutionary algorithms employed below, it is beyond the scope of the present work to examine in detail optimization algorithms. Instead, it will focus on creating suitable objective functions and then rely on routines contained in MATLAB's optimization toolboxes for minimization. For the rotated phase-space ellipse, MATLAB's `lsqnonlin` function [27] can be used to solve for a, b, and ψ in a least-squares fit. Figure 4.11 shows the outcome of this fit when applied to the tanh ramp used in the previous sections. The fit is done on turn 500 (more on this choice below).

We can thus define the objective function as the maximum absolute value of φ along the fitted ellipse. Since, for the scales used, the ellipse attains greater values in phase than in fractional energy deviation, this is equivalent to the projection of the fitted ellipse's major axis onto the phase axis, which we previously stated would be considered our bunch length, henceforth denoted as σ_b. In Fig. 4.11, $\sigma_b = 0.6867$. We now seek to minimize σ_b by optimizing the ramp function, subject to certain constraints.

The first of these constraints is that we will continue to assume a field that is ramped according to Eq. (4.15). That is, at turn number n, the neutrons see a field

$$B_g = \frac{1}{2} B_{g,max} \left[\tanh\left(slope\_factor \times \frac{n + offset - N_{ramp}}{N_{ramp}/2} \right) + 1 \right]$$

As in the previous sections, $B_{g,max}$ will be set to 1 T. That leaves N_{ramp}, $slope\_factor$, and $offset$ as the parameters to be varied in search of a global minimum. Since we can arbitrarily achieve better bunching by making the process slower and hence more adiabatic, we must

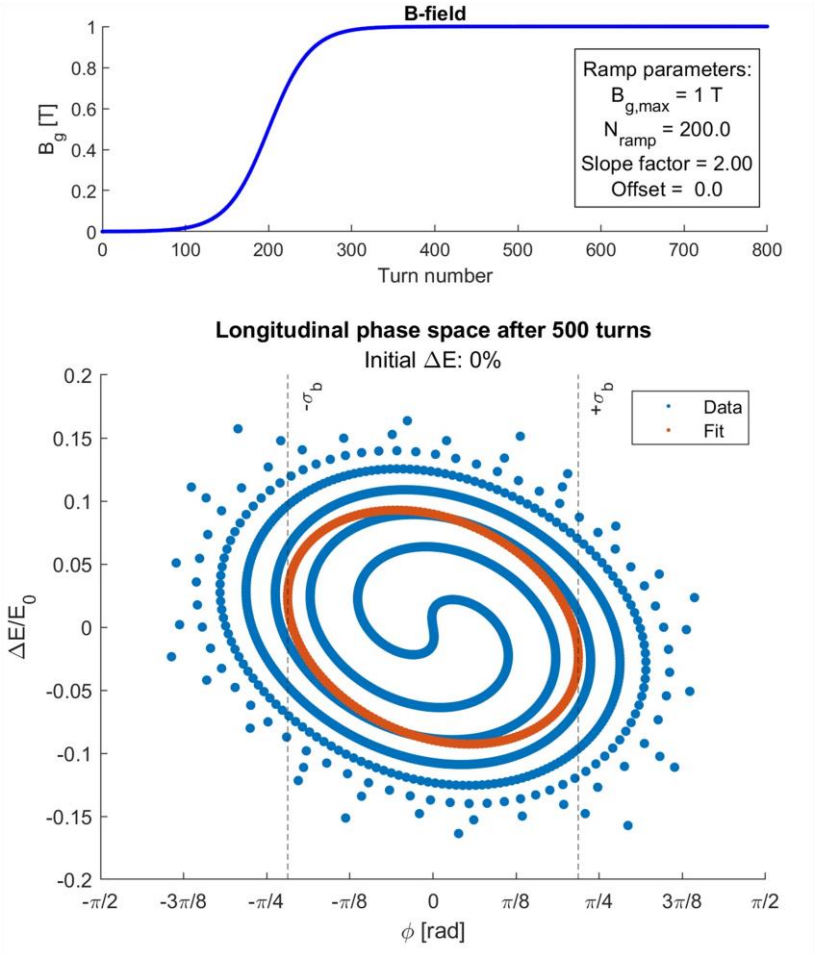

Figure 4.11: Phase-space ellipse fitted to the neutron bunch at turn 500 when using the manually optimized tanh-function ramp for adiabatic capture. The least-squares fit for the data results in $\sigma_b = 0.6871$.

also constrain the ramp function to complete the ramping process within a set amount of time. The original ramp function was manually optimized to finish ramping by turn 400; we therefore add the constraint that B_g must achieve at least 99.9% of $B_{g,max}$ by turn 400. If this constraint is not satisfied, then that combination of parameter values is penalized by being assigned the maximum possible bunch length (π).

This latter constraint creates discontinuities in the objective function. We can therefore only pursue gradient-free global minimization techniques. MATLAB's

`GlobalSearch` and `ga` functions both employ gradient-free algorithms belonging to the class of evolutionary methods (scatter search and genetic algorithm, respectively) [28, 29]; they differ in the heuristic used for generating trial points. The genetic algorithm approach is based on randomization, while scatter search is not [30]. Global minimization runs were carried out using both algorithms. It was found that the genetic algorithm more often found the lowest σ_b, although the advantage was typically only by about 0.2% to 0.5%.

Figure 4.12 shows an optimal ramp per the genetic algorithm under the 400-turn constraint, again fitted at turn 500. The minimum $\sigma_{b,400}$ found following several runs (to account for the randomization in the genetic algorithm) was 0.6510, or a 5.2% reduction in bunch length compared to the original manually optimized ramp. In fact, the algorithm found multiple ramps that could achieve this bunch length while satisfying the constraints. (The existence of multiple solutions would be the case for all optimizations.) The ramp shown in Fig. 4.12 uses the solution $N_{ramp} = 206.8413$, $slope\_factor = 1.8277$, and $offset = 2.2499$. The manually optimized bunch length $\sigma_{b,man}$ is also plotted for comparison.

As mentioned above, the constraint for the end of the ramping process is a significant factor in determining the smallest possible bunch length following adiabatic capture. Figures 3.13 (a) and (b) show the results of `ga`-based global minimization when B_g must achieve at least 99.9% of $B_{g,max}$ at turn 200 and turn 600, respectively. The faster ramp only reaches a minimum value of $\sigma_{b,200} = 0.9010$, while the slower ramp achieves $\sigma_{b,600} = 0.5401$. In both cases (and as above for the 400-turn constraint investigations), the phase-space ellipse is fitted at 100 turns past the prescribed end of the ramp. This ensures that the objective function reflects the effect of the ramp, without subjecting the bunches to varying amounts of time at maximum field. The latter would be the case if the phase-space ellipse is fitted at turn 800, for example, regardless of when the ramp finished.

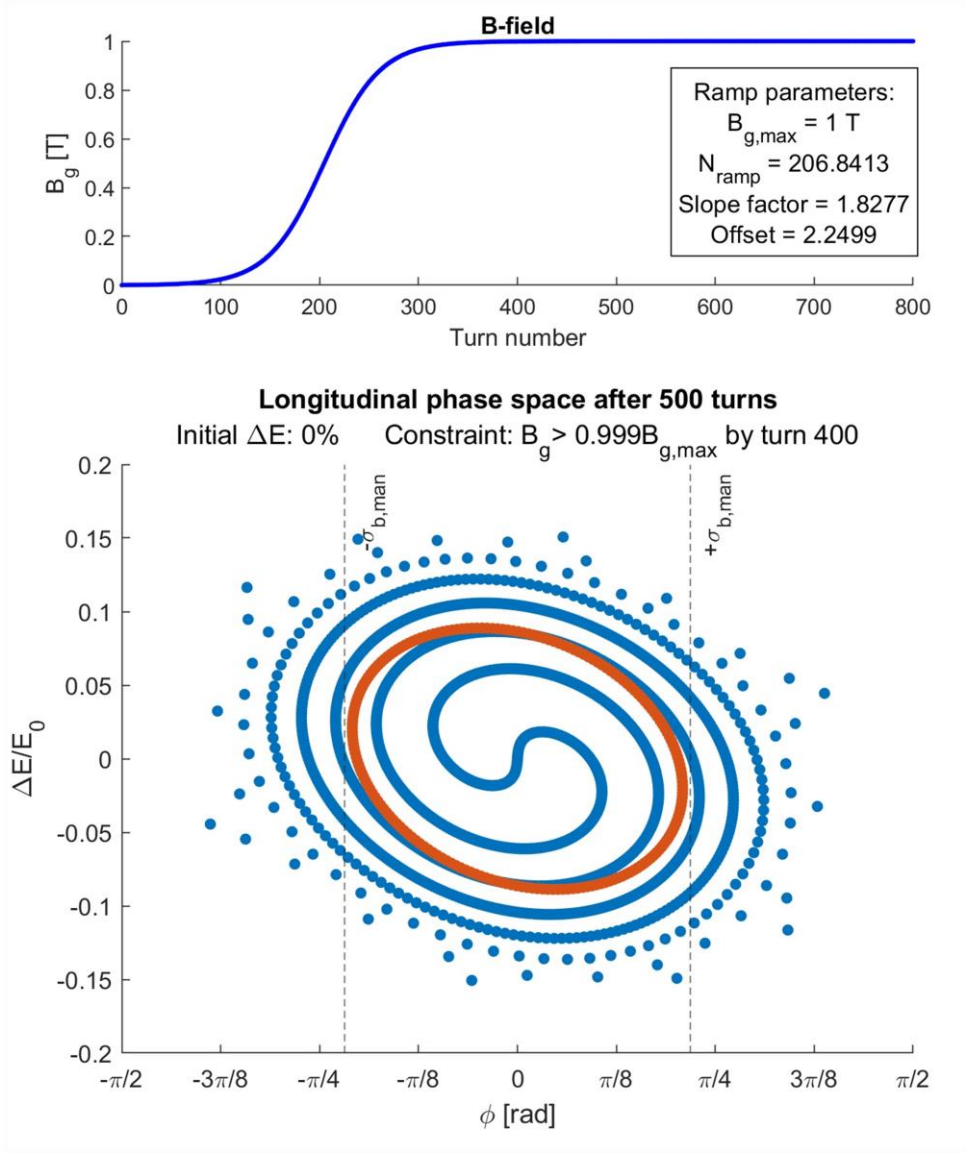

Figure 4.12: Optimal ramp parameters found by a genetic algorithm, subject to the constraint that ramping must be completed by turn 400 (i.e., B_g at turn 400 is greater than 99.9% of $B_{g,max}$). The bunch length at turn 500 for this numerically optimized ramp is 0.6510, as opposed to 0.6867 for the manually optimized ramp.

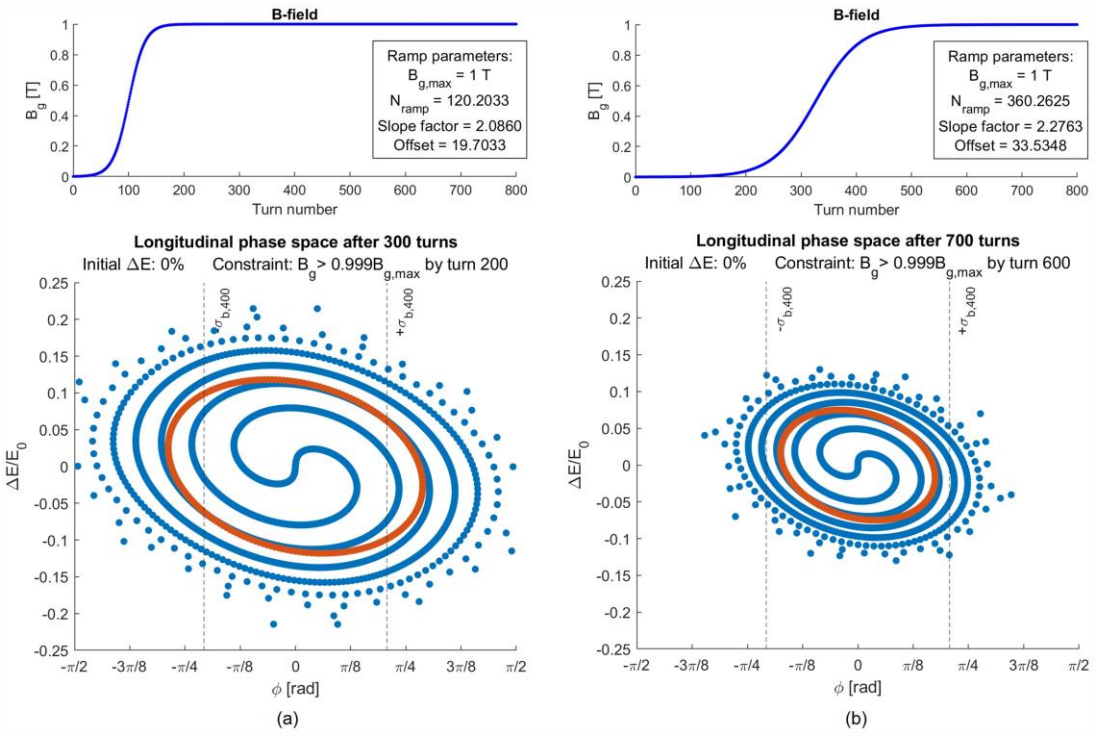

Figure 4.13: Minimum bunch length achieved when the ramp is optimized to finish within 200 turns (a) versus 600 turns (b). For (a), the value is 0.9010; for (b), it is 0.5401. The minimum achieved for the case of 400 turns is also plotted as $\sigma_{b,400}$.

4.4.2 Pareto front between bunch length and capture time

The results shown in Figs. 4.12 and 4.13 demonstrate the existence of a tradeoff between the minimum bunch length possible and the amount of time it takes to ramp the field to its maximum value. This tradeoff can be explored by generating the so-called Pareto front, which contains a set of optimal solutions to the corresponding multi-objective optimization problem [31]. Our objective function will now not only return σ_b, but also N_{end}, which is the turn number at which the ramp achieves 99.9% of $B_{g,max}$. The objective space is probed via

N_{ramp}, $slope\_factor$, and $offset$ as before. We again use a genetic algorithm—in this case, MATLAB's `gamultiobj` function to handle the two-objective function [32]. The resulting Pareto front is plotted in Fig. 4.14. The lack of kinks in the curve indicates good convergence in the set of optimal solutions. More encouragingly, the optimized values $\sigma_{b,200}$, $\sigma_{b,400}$, and $\sigma_{b,600}$ found in the previous section via global single-objective minimization all fall nicely on the curve. This curve can be inspected during any future work when seeking a balance between ramp time and bunch length when $B_{g,max} = 1\ T$.

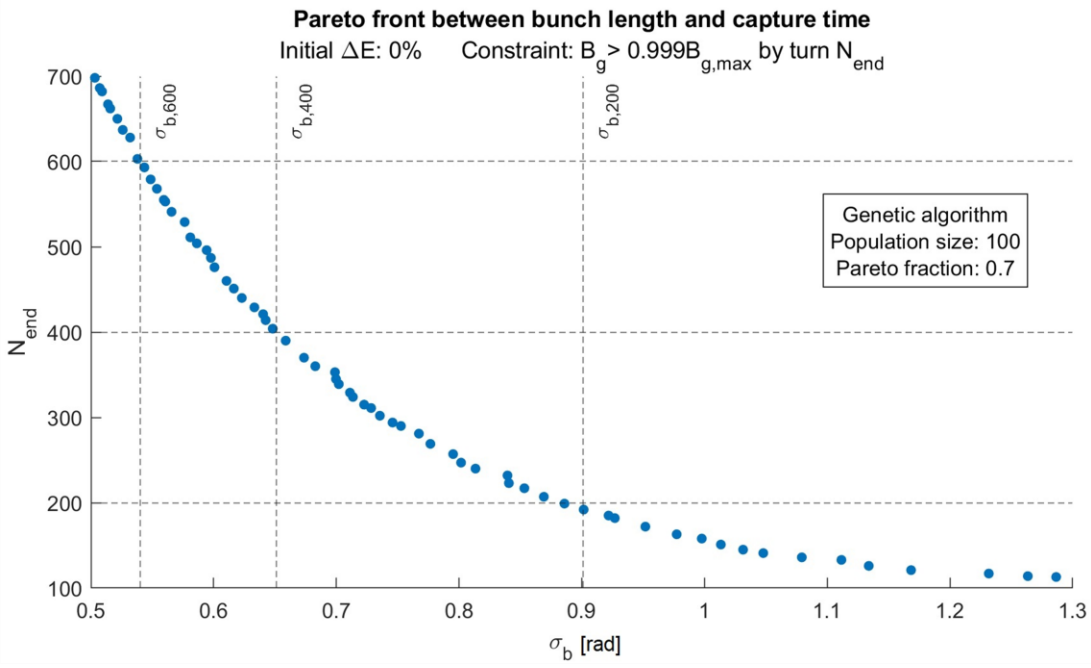

Figure 4.14: Pareto front between bunch length and capture time. The results of the global single-objective optimization problems of the previous section are also plotted as $\sigma_{b,600}$, etc., and show very good agreement with the curve. $B_{g,max} = 1\ T$.

4.4.3 Dynamic aperture versus maximum field

Given the realities of magnet engineering, it may be preferable to reduce $B_{g,max}$ below 1 T. Doing so would come at the cost of the dynamic aperture. Using the line-counting technique employed in Section 4.3.6, we can programmatically sweep across different values of $B_{g,max}$, count the uncaptured lines, and find the resulting numerical dynamic aperture when using the tanh ramp optimized for 400 turns. Figure 4.15 plots the results with 0.1% resolution in the dynamic aperture.

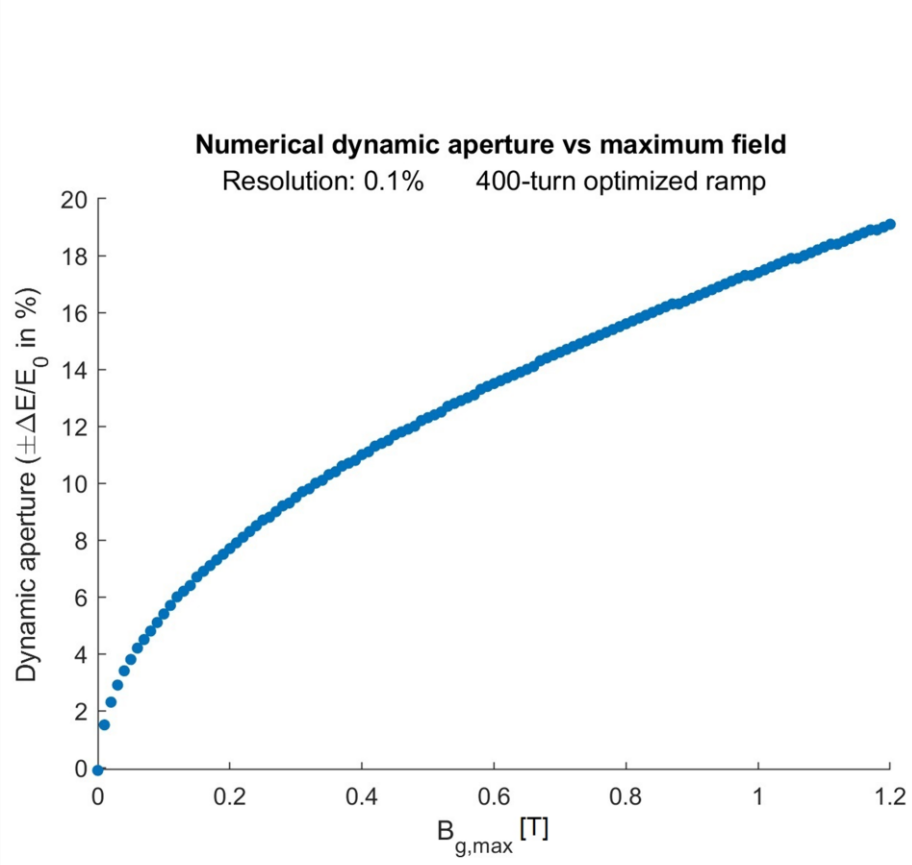

Figure 4.15: Numerical dynamic aperture vs maximum field $B_{g,max}$ as determined by counting off-energy levels captured by the bucket. The remaining ramp parameters in Eq. (4.15) are set to the $\sigma_{b,400}$-optimized values.

5 PRACTICAL DISCUSSION AND CONCEPTUAL DESIGNS

As stated previously, practical considerations were the dominating factor in the selection of parameters to use in the simulations. Higher-energy neutrons can be captured via the presented approach, but one must be mindful of the increasing demands on the magnets and supplies as one goes up in energy, possibly necessitating the use of superconducting magnets. The ring would also become larger. Another consideration to balance against the neutron energy would be the limitations imposed by the adiabatic condition together with the neutron lifetime: in order for the capture process to remain adiabatic, the ramping of B_g must not proceed too quickly turn by turn, but the whole process must be completed before most of the neutrons have decayed—and ideally with time to spare for experiments, whether performed in the ring or after the neutrons have been transported elsewhere.

For the system discussed, by far the greatest practical concern is the design of the AC dipole magnet. The present work requires a longitudinal field gradient, with essentially no transverse gradients, for this region and is predicated on a linear dependence of B_g on s. In Section 3.2.5, it was assumed that this linear dependence is achieved geometrically, by a B-field with separable components $C_g(s)$ and $I(t)$—the former being a fixed proportionality constant and the latter changing in time and being responsible for the actual ramp. See Fig. 5.1. The window-frame dipole magnet was given as an example of a B-field with the correct form. Returning to its equation, Eq. (3.35),

$$B_g(s,t) = \mu_0 \frac{N}{g} I(t)$$

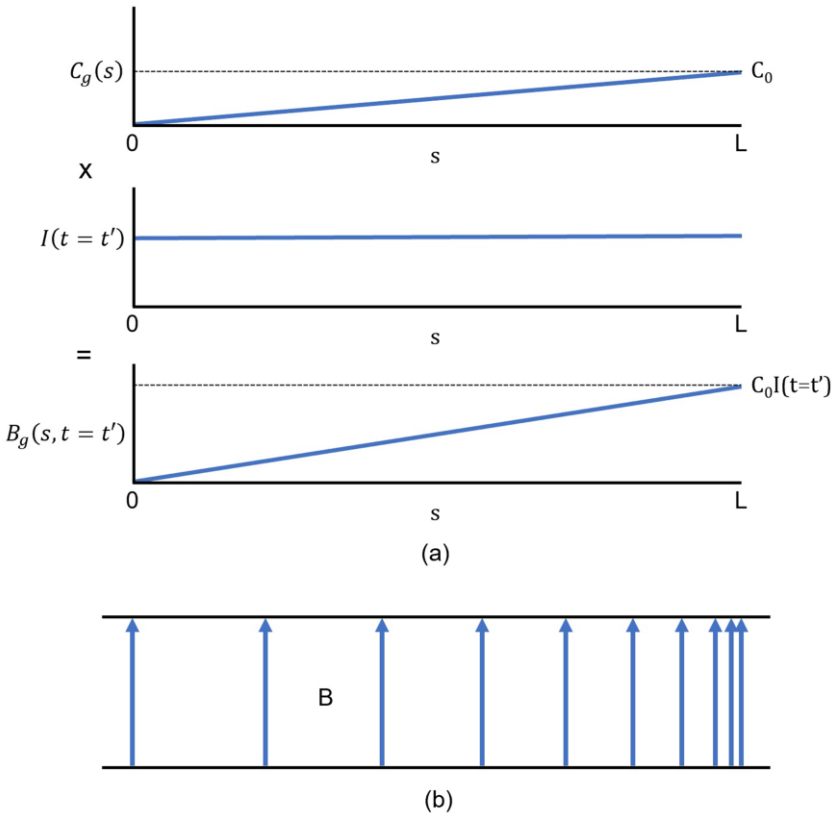

Figure 5.1: Achieving the required $B_g(s,t)$. (a) If $B_g(s,t)$ is the product of a linear function $C_g(s)$ and a time-dependent but s-independent current $I(t)$, then $B_g(s,t)$ can be ramped with time while preserving the required longitudinal gradient. (b) The required field has a longitudinal gradient but no transverse gradients.

we see that, to achieve $B_g(s,t) = C_g(s)I(t)$ with a gradient in s, N/g must vary with s. This can be achieved through N, g, or both. Practically speaking, g is best kept constant, which leaves N. As a reminder, in the above equation, N is the number of coil turns, g is the gap, and I is the current through each turn of coil.

The magnetic isolation needed for the ramping magnet also requires some attention. Since the time-varying field is purposely quasistatic for the sake of adiabaticity, high-

permeability metal alloys such as mu-metal will need to be carefully incorporated into the design. Faraday shielding will not be effective at such low frequencies.

Although the dynamic aperture found in Section 4.3.6 was $\pm 17.4\%$, the momentum acceptance of existing particle storage rings is generally $\pm 10\%$—that is to say, a physical realization of the system explored in the present work is currently most limited transversely, not longitudinally [33]. In order to realize the theoretical maximum in capture efficiency presented, the energy acceptance of the accompanying storage ring must match the dynamic aperture of the adiabatic capture. On this point, gravity becomes an especially important consideration in the lattice design, as the neutron's feeble interaction with electromagnetic fields and its sensitivity to Earth's gravitational field make it very susceptible to vertical orbit deviations. The attendant lattice is therefore another major practical consideration.

Following adiabatic capture, the bunched neutron beam can either remain circulating in the storage ring for experiments or exit to another storage ring or beamline(s) where experiments are then performed. The storage ring approach is an under-exploited opportunity, as a storage ring for neutrons has only been preceded by NESTOR [34], which did not have strong focusing and ceased operating in the 1980s. Many developments and advances have occurred since. One experimental setup that is easily attainable with storage rings is the use of distributed detectors. Because the neutron bunch will return to each detector location in a controlled, periodic manner, combined with thoughtful shielding, background noise can be well characterized. Both spin states could even be theoretically stored and observed simultaneously in counter-propagating rings sharing the same ramping magnet in a Figure-8 configuration, with a difference of π between their phases, but admittedly, such a design would be extremely ambitious and challenging.

6 SUGGESTIONS FOR FUTURE WORK

The present work has shown that neutron beams can be successfully bunched via adiabatic capture in simulations. However, the process has specific requirements regarding the fields and gradients; it furthermore must take place in the environment of a storage ring. Therefore, the most pressing future work would be related to the design of the ramping magnet and the storage ring lattice—both to ensure that the neutrons arrive at the magnet with acceptable transverse qualities and to capitalize on the maximum capture efficiency predicted by the simulations.

It may also be beneficial to explore other forms of $\frac{\partial B(s,t)}{\partial s}$ besides the linear one pursued in the present work in order to expand magnet design options. These new field geometries would then need to be followed by a new suite of simulations.

As demonstrated in Section 4.3.7, neutron storage rings are not immune to the nonlinearities and detrimental dynamics experienced by charged-particle rings—although they are fortunately spared the issue of wakefields. Thus, another very important area of future work would be on spin and betatron resonances. These investigations could be accompanied by the less pressing but still valuable study of higher harmonics.

Fortunately, the extensive existing body of work related to charged-particle accelerators and storage rings provides ample guidance for future work. The many outstanding problems involving neutron physics, meanwhile, provide ample cause for devising new experiments using bunched neutron beams and a neutron storage ring.

APPENDIX

The Maxwell(-Boltzmann) distribution is a special case of the Gamma distribution [35]. The probability density function (PDF) of the Maxwell distribution is given by

$$PDF_{Maxwell}(x) = A_1 x^2 e^{-\frac{x^2}{2\sigma^2}} \tag{A.1}$$

where A_1 is the normalization factor. The neutron flux, meanwhile, is given by [1]

$$\varphi_T = \frac{\varphi_0}{(kT)^2} E e^{-\frac{E}{kT}} \tag{A.2}$$

which does not look immediately Maxwellian, but noting that $E = \frac{1}{2}mv^2$, we see that it is Maxwellian in standard form in v.

The Gamma distribution is given by [36]

$$PDF_{Gamma}(x) = A_2 x^{a-1} e^{-\frac{x}{b}} \tag{A.3}$$

where a is called the shape parameter, b is called the scale parameter, and A_2 is the normalization factor. It is easy to see that Eq. (A.3) is equal to Eq. (A.2) for $a = 2$, $b = kT$, and $A_2 = \varphi_0/(kT)^2$. Therefore, to sample the distribution in E directly, one can use a Gamma random number generator. In MATLAB, for one sample of a neutron energy E_N, this appears as

```
E_N = gamrnd(2,kT)/1.6e-19
```

for energy in eV.

REFERENCES

[1] J. Byrne, *Neutrons, Nuclei and Matter: An Exploration of the Physics of Slow Neutrons*. Bristol, PA, USA: Institute of Physics Pub., 1995.

[2] D.T.L. Jones and A. Wambersie, "Radiation therapy with fast neutrons: A review," *Nucl. Instrum. Methods Phys. Res. A*, vol. 580, no. 1, pp. 522-525, 2007.

[3] F.E. Wietfeldt and G.L. Greene, "Colloquium: The neutron lifetime," *Rev. Mod. Phys.*, vol. 83, no. 4, pp. 1173-1192, 2011.

[4] J.S. Nico and W.M. Snow, "Fundamental neutron physics," *Annu. Rev. Nucl. Part. Sci.*, vol. 55, pp. 27-69, 2005.

[5] S. Paul, "The puzzle of the neutron lifetime," *Nucl. Instrum. Methods Phys. Res. A*, vol. 611, no. 2, pp. 157-166, 2009.

[6] R. W. Pattie *et al.*, "Measurement of the neutron lifetime using a magneto-gravitational trap and in situ detection," *Science*, vol. 360, no. 6389, pp. 627-632, 2018.

[7] F.M. Gonzalez *et al.,* "Improved neutron lifetime measurement with UCNτ," *Phys. Rev. Lett.*, vol. 127, no. 16, p. 162501, 2021.

[8] D. Dubbers and B. Märkisch, "Precise measurements of the decay of free neutrons," *Annu. Rev. Nucl. Park. Sci.*, vol 71, no. 1, pp. 139-163, 2021.

[9] S.K. Lamoreaux and R. Golub, "Experimental searches for the neutron electric dipole moment," *J. Phys. G: Nucl. Part. Phys.*, vol. 36, no. 10, p. 104002, 2009.

[10] C. Abel *et al.,* "Measurement of the permanent electric dipole moment of the neutron," *Phys. Rev. Lett*., vol. 124, no. 8, p. 081803

[11] D. Dubbers, "Particle physics with cold neutrons," *Prog. Part. Nucl. Phys.,* vol. 26, pp. 173-252, 1991.

[12] H. Abele, "The neutron. Its properties and basic interactions," *Prog. Part. Nucl. Phys.,* vol. 60, no. 1, pp. 1-81, 2008.

[13] Y. A. Alexandrov, *Fundamental Properties of the Neutron.* Oxford, UK: Clarendon Press, 1992.

[14] X. Kang, "The cooler injector synchrotron at IUCF," Ph.D. thesis, Phys. Dept., Indiana University Bloomington, Bloomington, IN, USA, 1998.

[15] NIST, CODATA Value: neutron magnetic moment, `https://physics.nist.gov/cgi-bin/cuu/Value?munn`, 2018.

[16] M. Daum *et. al.*, "First observation of trapped high-field seeking ultracold neutron spin states," *Phys. Lett. B,* vol. 704, no. 5, pp. 456-460, 2011.

[17] C.V. Sukumar and D.M. Brink, "Spin-flip transitions in a magnetic trap," *Phys. Rev. A*, vol. 56, no. 3, pp. 2451-2454, 1997.

[18] D.M. Brink and C.V. Sukumar, "Majorana spin-flip transitions in a magnetic trap," *Phys. Rev. A,* vol. 74, no. 3, p. 035401, 2006.

[19] S.Y. Lee, *Spin Dynamics and Snakes in Synchrotrons*. Singapore: World Scientific, 1997.

[20] S.Y. Lee, *Accelerator Physics.* Singapore: World Scientific, 2019.

[21] V. Toponogov, *Differential Geometry of Curves and Surfaces: A Concise Guide.* Boston, MA, USA: Birkhäuser, 2006.

[22] H. Goldstein, C. Poole, and J. Safko, *Classical Mechanics.* San Francisco, CA, USA: Addison Wesley, 2002.

[23] W. Magnus and S. Winkler, *Hill's Equation.* New York, NY, USA: Interscience Publishers, 1966.

[24] V.I Arnold, *Mathematical Methods of Classical Mechanics*. New York, NY, USA: Springer-Verlag, 1989.

[25] R.L. Workman *et al.* (Particle Data Group), "Review of Particle Physics," *Prog. Theor. Exp. Phys*., vol. 2022, no. 8, 083C01, 2022.

[26] S.Y. Lee, private communication, Jan. 2023.

[27] MathWorks, Solve nonlinear least-squares (nonlinear data-fitting) problems – MATLAB & Simulink, `https://www.mathworks.com/help/optim/ug/lsqnonlin.html`.

[28] MathWorks, How GlobalSearch and MultiStart Work – MATLAB & Simulink, `https://www.mathworks.com/help/gads/how-globalsearch-and-multistart-work.html`.

[29] MathWorks, Find minimum of function using genetic algorithm – MATLAB & Simulink, `https://www.mathworks.com/help/gads/ga.html`.

[30] F. Glover & M. Laguna, "Fundamentals of Scatter Search and Path Relinking," *Control and Cybernetics*, vol. 29, no. 3, pp. 653-684, 2000.

[31] MathWorks, Find Pareto front of multiple fitness functions using genetic algorithm – MATLAB & Simulink, https://www.mathworks.com/help/gads/gamultiobj.html.

[32] MathWorks, gamultiobj Algorithm – MATLAB & Simulink, https://www.mathworks.com/help/gads/gamultiobj-algorithm.html.

[33] S.Y. Lee, private communication, Mar. 2023.

[34] K.-J. Kügler *et al.,* "NESTOR – A magnetic storage ring for slow neutrons," *Nucl. Inst. Methods Phys. Res. A,* vol. 228, no. 2, pp. 240-258, 1985.

[35] Wolfram Research (2007), MaxwellDistribution, Wolfram Language function, https://reference.wolfram.com/language/ref/MaxwellDistribution.html (updated 2016).

[36] Wolfram Research (2007), GammaDistribution, Wolfram Language function, https://reference.wolfram.com/language/ref/GammaDistribution.html (updated 2016).